DEFORMATION MECHANISMS AND MICROSTRUCTURES OF EXPERIMENTALLY DEFORMED MAGNESITE

A Thesis

by

CHRISTOPHER ANDREW ULRICH

Submitted to the Office of Graduate and Professional Studies of
Texas A&M University
in partial fulfillment of the requirements for the degree of

MASTER OF SCIENCE

Chair of Committee,	Andreas Kronenberg
Committee Members,	Julie Newman
	Zoya Heidari
Head of Department,	Mike Pope

December 2015

Major Subject: Geology

ABSTRACT

Carbonates may be incorporated in the mantle at collisional plate boundaries by many processes, including subduction of weathered oceanic lithosphere and fault-bounded tectonic slivers of seamounts. Once magnesite is formed in subducting slabs, it is likely to remain as an important carbon-bearing phase, as its stability extends over a wide range of mantle conditions. High-magnesium carbonates, including magnesite and dolomite, have been observed in ultra-deep metamorphic collisional terrains and in mantle xenoliths. Recent deformation experiments of magnesite indicate that it is weaker than mantle phases such as olivine and that it is likely to affect the geodynamics of subduction. Microstructures and lattice orientations of experimentally deformed samples have been investigated in this study, using optical and electron microscopes and electron backscatter diffraction. Microstructures of samples deformed at lower temperatures (400-600 ˚C), at strain rates of 10^{-4}-10^{-6} s^{-1} and an effective pressure of 900 MPa are dominated by undulose extinction, kink bands, and mechanical twins. At higher temperatures (>750 ˚C), microstructures include undulatory extinction and extensive dynamically recrystallized grains, subgrains, and core-and-mantle structures. Mechanical twins are not observed at these higher temperatures. External rotations of magnesite c- and a-axes show that dislocations glide on the c, r, and f planes by slip systems that are similar to those reported for calcite and dolomite. Additionally, magnesite mechanically twins on the e- and f-planes. The CRSS values for magnesite twins exceed 300 MPa, significantly greater than twinning CRSS reported for either calcite or dolomite. I

propose that twinning CRSS in the carbonate system is controlled, not by crystal class or cationic ordering, but by cationic size, which affects CO_3^{2-} anion-anion repulsion at twin boundaries. This hypothesis is consistent with lowest energy calcite twin modeling of Bruno et al. (2010). In a similar fashion to twinning, I predict that dislocation movement is also controlled by cation size. Lastly, I observe that this effect is not limited to carbonates. Cationic size may also affect CRSS values for twinning in oxides and the strength of olivine with different Fe and Mg contents deforming in the dislocation creep regime.

ACKNOWLEDGEMENTS

I would like to thank my committee chair, Dr. Kronenberg, and my committee members, Dr. Newman and Dr. Heidari, for their guidance and support throughout the course of this research. I would specially like to thank Dr. Holyoke III for enormous amount of time and effort he dedicated to mentoring me. Know that your help has changed my life. I would also like to thank Dr. Guillemette for his time and expertise on the Microprobe. Thanks also go to my friends and colleagues and the department faculty and staff for making my time at Texas A&M University a great experience. I also want to extend my gratitude to the National Science Foundation, which provided the funding for my project. Finally, thanks to my mother, father, and stepfather for their guidance and encouragement and to my friends for helping me through it all.

NOMENCLATURE

ε	Strain
ε̇	Strain rate
A	Pre-exponential constant
σ	Stress
d	Grain size
n	Stress exponent (material constant)
m	Grain size exponent (material constant)
Q	Activation energy
R	Universal gas constant
T	Temperature
P	Pressure
GBM	Grain boundary migration
SGR	Sub-grain rotation
SEM	Scanning electron microscope
SE	Secondary electron mode
BSE	Backscattered electron mode
EBSD	Electron backscattered diffraction mode
LPO	Lattice preferred orientation
U-stage	Universal stage petrographic microscope

TABLE OF CONTENTS

Page

1. INTRODUCTION

Carbonates may be incorporated in the mantle at collisional plate boundaries by many processes, including subduction of weathered oceanic crust and mantle (Plank and Langmuir, 1998; Kerrick and Connolly, 2001; Zhu and Ogasawara, 2002) and fault-bounded tectonic slivers of seamounts (Wada et al., 1994; Bashir et al., 2009). Magnesite can be formed in the mantle by reaction with CO_2-rich fluids, and it is commonly found within serpentinized peridotite bodies (Kushiro, 1975). Once magnesite is formed in subducting slabs, it is likely to remain as an important carbon-bearing phase, as its stability extends over a wide range of mantle conditions. Oceanic carbonaceous sediment, primarily calcite and dolomite, comprise a large portion of total oceanic sediment (~7%) (Plank and Langmuir, 1998). When subducted, these carbonates serve as a significant source of carbon in the mantle. At depth, calcite and dolomite react to form magnesite (Biellmann et al., 1993); which is stable throughout much of the mantle (Gillet, 1993). High-magnesium carbonates have been observed in ultra-deep metamorphic collisional terrains and in mantle xenoliths (Dobrzhinetskaya et al., 2006; Sato and Katsura, 2001). The presence of magnesite in subduction zones may be important to the geodynamics of downgoing slabs, given that its mechanical properties differ from those of olivine and other mantle silicates.

Magnesite is weak relative to the strengths of most mantle silicates. Thus, its presence within subduction zones may reduce resistance forces to subduction. In the crust, calcite is weak compared with the strengths of quartz (Hirth and Tullis, 1992) and

feldspars (Tullis and Yund, 1985). In the mantle, magnesite is weak relative to olivine and pyroxenes (Holyoke et al., 2014). The crystal structure of magnesite is the same as that of calcite, with Mg substituting for Ca, and the same CO_3 layers. Both magnesite and calcite are rhombohedral and have the same crystal symmetry ($R\bar{3}C$). Recent experiments of Holyoke et al., 2014 provide deformed samples for this study at controlled conditions. The mechanical results show that magnesite is markedly weaker than olivine at all mantle depths and may serve to localize deformation and reduce viscous resistance forces in subducting slaps. Through interconnection and localization (Holyoke and Tullis, 2006), magnesite may act as a strength-controlling phase in subducting slabs. This study will contribute to our understanding of the rheology of magnesite by determining the mechanisms of deformation, fabric, and microstructural changes that are likely to be important at subduction zone conditions.

Of the rhombohedral carbonates of the Mg-Ca system, only calcite and dolomite have been well studied. Due to the prevalence of these carbonates in the crust and involvement in collisional tectonics, the deformation of calcite and dolomite has been studied extensively. Early experimental work focused on deformation of calcite polycrystalline aggregates, including marbles, limestones, and synthetic aggregates (Griggs and Miller, 1951; Handin and Griggs, 1951; Turner and Ch'ih, 1951; Griggs et al., 1951; Griggs et al., 1953; Borg and Turner, 1953; Turner et al., 1956) as well as single crystals (Braillon et al., 1978; De Bresser and Spiers, 1990; De Bresser and Spiers, 1993; Turner et al., 1954; Wang et al., 1996).

Schmid et al., 1980 described three deformation regimes in calcite and differentiated them based on experimentally derived material constants resulting from the Arrhenius relationship. The relationship, first applied to calcite by Heard and Raleigh, 1972, relates strain-rate to temperature, stress, and grain size and is as follows:

$$\dot{e} = A\sigma^{n} d^{-m} exp^{-Q/RT}$$

where $\dot{e}$ is strain rate, A is the pre-exponential constant, σ is stress, d is grain size, n and m are material constants, Q is activation energy, R is the gas constant, and T is temperature. Schmid et al., 1980, characterized the first as a low-temperature crystal-plastic regime based on its relatively low strain-rate dependence. The second regime is consistent with dislocation creep with a high stress exponent, $n = 7 – 8$, in which grains are deformed at their margins with a characteristic "core and mantle" microstructure. The third regime is also consistent with dislocation slip, but mechanical results yield a much lower stress exponent, $n < 4$, and grain boundary migration appears to be more extensive.

The power-law constitutive equation (above) is not the only flow law that can be used to describe crystal-plastic deformation. Analyses by Renner et al., 2002 show that under some conditions dislocation creep may operate in conjunction with diffusion creep; observing that n and Q are dependent on stress, grain size, and temperature. To reconcile these variations in n and Q, they used a Peierls law:

$$\dot{\varepsilon}_p = A_p \sigma^2 \exp\left(\frac{\sigma}{\sigma_p}\right) \exp\left(\frac{-Q_p}{RT}\right)$$

where A_p is a material constant, Q_p is the activation energy, σ_p is the resistance to dislocation glide, and other variables are as above. The resistance to dislocation glide, σ_p, can be determined by:

$$\sigma_p = (\sum p, 0 + Kd^{-m})(T_m - m)$$

where $(\sum p, 0 + Kd^{-m})$ is the intrinsic Peierls stress and $\sum p, 0\ (T_m - m)$ is backstress. Unlike Schmid et al., 1980, Renner et al., 2002 and many others who inferred that deformation was primarily accommodated by dislocation movement, De Bresser, 2002 proposed that deformation in this regime may be primarily accommodated by cross-slip deformation. Using this assumption, he applied a constitutive equation for cross-slip given by:

$$\dot{\epsilon} = K' \left(\frac{\sigma}{\mu}\right)^2 exp\left[-\frac{\Delta U_{cs}(\sigma, P)}{kT}\right]$$

where K' is a material constant, $\Delta U_{cs}(\sigma, P)$ is the energy required to overcome an obstacle, influenced by external stress σ and external pressure P, and all other variables are as above.

The mechanical behavior and the resulting microstructures produced in the low temperature crystal plastic regime have been extensively characterized since the early Yule marble experiments. Calcite mechanically twins on $e \equiv \{01\bar{1}8\}$, $r \equiv \{10\bar{1}4\}$, and $f \equiv \{01\bar{1}2\}$, and slips on $r \equiv \{10\bar{1}4\}$ in $\langle\bar{2}021\rangle$ directions, $f \equiv \{01\bar{1}2\}$ in $\langle02\bar{2}1\rangle$ directions, and $c \equiv \{0001\}$ in $\langle2\bar{1}\bar{1}0\rangle$ directions (Barber, 1977; Busch and Van der Pluijm, 1995). Calcite twins have been used to calculate exact strains and principal stress orientations (Groshong, 1972) and more recently, twin geometries which exhibit

boundary migration have been used as a calcite geothermometer (Burkhard, 1993; Ferrill et al., 2004).

The dislocation creep regime of calcite has seen extensive research in the last forty years; with studies on the mechanical behavior (Heard and Raleigh, 1972; Schmid et al., 1980; De Bresser, 2002; Renner et al., 2002), the microstructures (Schmid et al., 1987; Fredrich et al., 1989; Pieri et al., 2001), and the internal recovery mechanisms such as climb (Schmid, 1976; Barber and Wenk, 2001) or cross-slip (De Bresser et al., 2005; Barber and Wenk, 2001). The type of dislocation-assisted recrystallization that is active characterizes this regime. One type of recrystallization, subgrain rotation recrystallization (SGR), involves dislocation climb, a solid-state diffusion recovery mechanism. However, recent work postulates that recovery in this regime may be driven by cross-slip instead of dislocation climb (De Bresser and Spiers, 1990). The dominant recovery mechanism in this regime continues to be an area of much disagreement today.

Subgrain rotation (SGR) recrystallization is a process by which recrystallization is driven by the continuous addition of dislocations to subgrain boundaries, resulting in a misorientation of the subgrain crystal lattice. Grain boundary migration (GBM) recrystallization is a process by which recrystallization is accommodated by SGR processes as well as through movement at grain boundaries from areas of low dislocation densities into areas of high dislocation densities.

Numerous recent advances have been made in the calcite dislocation creep regime. Rutter and Elliott, 1976 investigated lattice preferred orientation development within dynamically recrystallized calcite grain. Bresser et al., 2001, using concepts

pioneered by Twiss (1977) created a calcite piezometer based on recrystallized grain size, and Herwegh et al. (2005) attempted to rectify discrepancies between experimentally derived flow laws and microstructural field observations.

The diffusion creep regime of calcite has also seen significant interest in the last few decades. The mechanics (Rutter and Elliott, 1976; Schmid, 1976) and the microstructures (Schmid et al., 1980; Schmid et al., 1987; Casey et al., 1998) of calcite in the diffusion creep regime have been the focus of much interest. Additional work (Bresser et al., 2001, Paterson and Olgaard, 2000) has examined rheological weakening by way of grain size reduction resulting from a transition from dislocation creep to diffusion creep. Instead of an abrupt switch in mechanism from the grain size insensitive dislocation creep regime to the grain-size sensitive diffusion creep regime, they observed that a balance developed between grain size reduction mechanisms and grain growth mechanisms. Additionally, high experimental shear strain experiments of calcite (Casey et al., 1998; Paterson and Olgaard, 2000; Pieri et al., 2001; Rybacki et al., 2003) enabled study of large-strain transient creep and deformation to steady-state creep.

The deformation of dolomite has been studied in naturally deformed rocks (House and Gray, 1982; Newman and Mitra, 1993; Billi and Di Toro, 2008; Fondriest et al., 2012) as well as in experiments (Higgs and Handin, 1959; Neumann, 1969; Barber et al., 1981; Barber et al., 1994; Barber and Wenk, 2001). However, at low temperatures and pressures of the upper crust, dolomite deforms largely by brittle mechanisms (Heard, 1976; Handin and Hager Jr., 1957) and high temperature rheologies have only recently been reported (Davis et al., 2008; Delle Piane et al., 2008). Dolomite exhibits

mechanical twinning and slip; however unlike calcite, mechanical twinning of dolomite occurs predominantly on $f \equiv \{01\bar{1}2\}$ (Barber and Wenk, 1979) and dislocation slip occurs on $c \equiv \{0001\}$ in $\langle 2\bar{1}\bar{1}0\rangle$ directions and $f \equiv \{\bar{1}012\}$ in $\langle \bar{2}20\bar{1}\rangle$ directions (Barber et al., 1981). Additionally, the dolomite grain growth rate (in diffusion creep) is orders of magnitude slower than that of calcite (Davis et al., 2011).

Due to its relatively low abundance in the crust, very few studies have investigated naturally deformed magnesite (Ibarguchi, 1999); Sasvári and Kondela (2007)). In both of these studies, little analyses were done to describe deformation and no microstructural observations were made. Additionally, only one study has explored the mechanics of experimentally deformed magnesite Holyoke et al., 2013. Holyoke et al., 2013 found that magnesite is stronger than both calcite and dolomite at crustal conditions; where magnesite deforms largely by brittle mechanisms. At higher temperatures, magnesite deforms via crystal plastic deformation mechanisms (i.e. diffusion creep and/or dislocation creep) and eventually becomes the mechanically weakest of all the common carbonates (Holyoke et al., 2013). Magnesite is also orders of magnitude weaker than olivine at all conditions within the mantle. Holyoke et al., 2013 postulate that the significant strength disparity between magnesite and olivine may promote deep focus earthquakes through ductile instabilities. A recent study by Davis et al., 2011 has shown that the grain growth rate (diffusion creep) of magnesite is markedly slower than that of calcite. Dolomite grain growth was thought to be slow in comparison to calcite due to its complex cationic layering. However, results from Davis et al., 2011

imply that the change from a calcium cation to a magnesium cation may be far more chemically influential on rate than previously thought.

While mechanical twinning has been reported for both calcite and dolomite, no twin laws have been reported for magnesite. The only reference to translational gliding appears in Higgs and Handin, 1959 and is based on inferences made by Johnsen, 1902. Due to crystallographic similarities, I hypothesize that the twin laws and slip systems of magnesite might be the same as those observed in calcite and/or dolomite.

2. MAGNESITE SAMPLES AND RHEOLOGICAL RESPONSE

Samples selected for this microstructural study were deformed experimentally by Holyoke et al., 2014 in a study of the rheologies of magnesite. Coarse-grained samples deformed at T = 400 – 1000 ˚C, strain rates $\dot{\varepsilon} = 10^{-7} - 10^{-4}$/s, and an effective pressure of 900 MPa were examined by optical microscopy, SEM, TEM, and EBSD to identify mechanisms of deformation and characterize resulting deformation microstructures and fabrics.

2.1 Starting materials

The coarse-grained magnesite used in the rheological study by Holyoke et al., 2014 is from Nevada, USA (**Figure 1**), has an average grain size of ~100 μm, very low porosity (<1%), and rare inclusions (<<1%) of ultramafic or altered ultramafic materials. This magnesite aggregate contains extremely small amounts of Ca and Fe ($Mg_{0.994}Ca_{0.004}Fe_{0.002}CO_3$); thus it is very close to an ideal end-member magnesite composition. Grains of the aggregate are equant, show straight extinction between crossed polarizers, and are free of twins. For a more detailed description of the undeformed starting material, see Holyoke et al., 2014.

2.2 Experimental assembly/apparatus

All experiments were performed using solid or molten salt assemblies in a Griggs

deformation apparatus (Figure 2a). The apparatus utilizes solid (Figure 2b) or molten (Figure 2c) salt confining media to reach confining pressures up to 2000 MPa and temperatures up to 1300 ˚C. For a more detailed discussion of the experimental assembly and apparatus used in the deformation of these magnesite samples, see Holyoke et al., 2014. Temperatures are known to within < 10˚C and differential stresses are known to within +/- 2 MPa. Confining pressures P_c were applied at a given temperature to result in an effective pressure P_e of 900 MPa, assuming that $P = P_c - P_{CO2}$ where the CO_2 pressure was taken to be the equilibrium value at a given temperature reported by Goldsmith et al. (1955).

2.3 Rheological response

In all experiments, differential stresses increase quickly with strain, reaching the elastic limit, and then deformed inelastically. At low temperatures ($T \leq 600$ ˚C), samples undergo significant work hardening post yielding. At intermediate and high temperatures ($T \geq 700$ ˚C), samples reach relatively constant (steady state) differential stresses by 5-10% strain, and change little at strains of up to 28%.

3. METHODS

To study the microstructures of the deformed magnesite, each sample was quenched and unloaded over the course of an hour at the termination of each deformation experiment. After quenching, each sample was allowed to further cool to room temperature overnight, removed from the assembly, and impregnated with epoxy. The epoxy was allowed 24 hours to set and then each sample was cut along a plane parallel to the direction of maximum compressive stress. A doubly-polished ultra-thin section (<2-4um) was prepared from each sample for optical and SEM analyses.

3.1 Thin section preparation

Due to the extremely limited volume of sample available for study, all thin sections were prepared by hand, in-house. Deformed cylinders were cut along a plane parallel to the maximum compressive stress (σ_1). For each sample, the surface of one of the half-cylinders was then polished using alumina grit of decreasing grit size (down to 0.3 um). Each polished half-cylinder sample was sonicated for 10 minutes to remove any residual grit and then baked on a hot plate at 145 ˚C for 12 hours to ensure the expulsion of all water from within the sample. The cylinders were then epoxied, polished-side down, to cleaned thin section glass plates and allowed to set for 12 hours. The cylinders were then cut using a Buehler Isomet low speed saw such that only thin wafers of rock (<300 μm) were left attached to the thin section. The samples were then thinned carefully to 2-4 μm and polished.

3.2 Microstructural characterization

Optical deformation microstructures of each sample were characterized optically using a Nikon Eclipse LV100POL petrographic microscope. Scanning electron microscopy (SEM) of polished surfaces was carried out using a FEI Quanta 600 microscope. Rotation of c-axes was determined optically using a 5-axis universal (u) stage, and a- and c-axis orientations were determined electron backscatter diffraction (EBSD) using on the FEI Quanta 600 SEM. EBSD data were processed using Flamenco (Channel 5, Oxford Instruments) to create stereoplots that illustrate lattice-preferred orientations. For all samples, only the central portion was studied to eliminate errors associated with stress variations resulting from end-effect stress distributions. Twin laws and slip systems were evaluated using both optical u-stage measurements and EBSD SEM measurements. External rotations of crystallographic axes were used to identify the slip systems of magnesite using methods used by Turner et al. (1954) to evaluate the slip systems of calcite. The mechanical twins of magnesite were characterized by determining their boundaries relative to the c-axis. Slip was characterized using optical u-stage methods and determining the change in a- and c-axis orientations using EBSD.

3.3 Grain size analysis

Photomicrograph-mosaics (20x magnification) were used to trace >500 grains in each sample to be used in grain-size analyses. Grain tracings were analyzed by methods used by Herwegh et al., 2005 for deformed calcite, using the grain size analysis program

NIH image 1.62 to determine the average of the grain diameters and chord lengths (D), grain size distributions, grain aspect ratios (b/a), and grain shape preferred orientations (SPO).

4. RESULTS

4.1 Microstructural observations

Optical and scanning electron microscopy reveal a variety of deformation microstructures. These microstructures include undulatory extinction between crossed polarizers, mechanical twins, fractures, kink/deformation bands, subgrains, dynamically recrystallized grains, and core-and mantle recrystallization structures. In general, I observe that at low and intermediate temperatures, most grains exhibit undulatory extinction; some of those grains additionally contain sharply defined boundaries separating one zone of undulatory extinction from another. At low and intermediate temperatures, I observe a monomodal grain size, with the average grain size ~50 μm. At high temperatures, I observe a trimodal grain size distribution, with the largest grain size ~20 μm, the intermediate grain size ~5 μm, and the smallest grain size 2 μm. Like low and intermediate temperatures, the majority of grains exhibit undulatory extinction. However, the extinction observed is much more sweeping that at lower temperatures. Additionally, undulatory boundaries separating one extinction pattern from another are observed within grains. However, these boundaries are far less sharply defined than in grains deformed at lower temperatures.

In my initial examination of the thin sections, I also observed that every sample contained at least one through-going shear zone oriented 30-45˚ to σ_1. The orientation of these shear zones (~30˚ to σ_1), as well as the prevalence of distributed deformation, led me to believe that these zones were formed during pressurization of samples and did not

contribute substantially to strains at experimental conditions. Therefore, I chose to investigate microstructures outside of these fracture zones.

4.2 Deformation and recovery processes linked to rheology

Holyoke et al. (2013) characterized two distinct mechanical regimes for coarse-grained magnesite, deformed at constant strain rate at temperatures of 400-1000 ˚C. Flow strengths depend weakly upon temperature at temperatures ≤600 ˚C (Q – 229 kJ/mol) and depend on strain rate ($\dot{\varepsilon}$) by a nearly plastic $\sigma - \dot{\varepsilon}$ relation (n = 19.7 assuming a power law $\dot{\varepsilon} \propto \sigma^n$). In contrast, flow strengths depend strongly on temperature at temperatures ≥800 ˚C (Q - 410 kJ/mol) and they depend on strain rate according to a power law $\dot{\varepsilon} - \sigma$ relation where n = 3. Microstructural observations of the deformed samples reveal these distinct regimes, from deformation microstructures associated with crystal plastic deformation and little or no recovery at low T (400-500 ˚C), deformation mechanisms characteristic of dislocation at high T (800-1000 ˚C) and transitional deformation microstructures at intermediate T (600-750 ˚C).

4.2.1 Crystal plastic deformation microstructure of 400-500 ˚C samples

The optical microstructures of samples deformed at temperatures of 400 ˚C and 500 ˚C show that deformation is accomplished by multiple crystal plastic processes. Observation of kink bands (Figure 4a) and undulatory extinction (Figure 4a) indicate deformation via dislocation glide and, mechanical twinning (Figure 4a), on e and f planes. These deformation microstructures correspond to a strain-hardening mechanical

response that is indicative of little to no operative recovery mechanisms. Microcracks are apparent at grain boundaries and across individual grains. However, relatively little scattering of light is noted in plane-polarized light, indicating that microcracking is limited and plays a secondary role to the total finite strain relative to crystal plastic mechanisms.

These microstructures suggest that dislocation slip, brittle fracture, and twinning mechanisms were all active during deformation at these temperatures. At these temperatures, most grains exhibit undulatory extinction. However, only a few well-oriented grains exhibit mechanical twins. This suggests that the dominant mechanism at these temperatures is dislocation glide. No evidence is found for recovery, either within grains or at grain boundaries; optical subgrain boundaries are lacking, and the grain boundaries of original grains lack evidence of recrystallization.

Lattice preferred orientations (LPOs) with c-axes aligned with the shortening direction and a wide range of a-axis orientations perpendicular to the shortening direction (Figure 6) are consistent with glide on c, e, f, and r planes, though at these temperatures LPOs are only slightly stronger than that of the starting material (Figure 5). In the absence of recrystallization, the mean grain sizes of these samples (Figure 8) are roughly the same as the starting material. These microstructures and fabrics correspond to high differential stresses (930-1200 MPa) and strain hardening, measured at $T \leq 500$ $^{\circ}$C and strain rates of 10^{-4} to 10^{-7} s^{-1} (Holyoke et al. (2014)).

4.2.2 Transitional deformation microstructures of 600-750 ˚C samples

Optical microscopy of Nevada magnesite samples deformed at temperatures between 600-750 ˚C reveals that dislocation slip is more homogenously distributed throughout individual samples; most grains exhibit undulatory extinction and many grains exhibit kink/deformation bands (Figure 4b). Mechanical twins and microcracks are absent. Samples deformed at these conditions do not exhibit optical subgrains and few recrystallized grains, within grains or at grain boundaries, are observed. I infer that dislocation glide with limited recovery and recrystallization dominates deformation throughout this regime. Thus, deformation at these temperatures marks a transition from dislocation glide to dislocation creep.

The formation of an LPO (Figure 7) with c-axis maxima parallel to the compressive direction, and a-axes in a broad girdle perpendicular to the compressive direction provides evidence for dislocation glide, possibly on c, f, and r planes.

These microstructures and fabrics correspond to moderate differential stresses (700-1060 MPa), slight strain hardening (3-6%), followed by steady state deformation at 600˚ ≤ T ≤ 750 ˚C (Holyoke et al. (2014)). The steady-state mechanical response is consistent with my interpretation that dislocation glide is operating in conjunction with reductions in dislocation density near margins of original grains by recrystallization.

4.2.3 Dislocation creep microstructures of 800-1000 ˚C samples

Magnesite grains of samples deformed at high temperatures (>800 ˚C) exhibit extensive dynamic recrystallization at grain boundaries (Figure 4c), defining a core-and-mantle

structure. High magnification (Figure 4d) optical microscopy reveals sutured grain boundaries and well-developed subgrains within coarse, original grains. Recrystallized grains are also observed in porphyroclast interiors (with sizes of 1.9-2.5 μm). These grains are finer than the recrystallized grains (with sizes of 1-2 μm) found at boundaries of coarse, original grains. Deformation bands within grains are broader than those formed at lower temperatures and undulatory extinction is more sweeping. No twins were observed in any of these samples, and I attribute occasional cracks observed in these samples to unloading at the termination of the experiments. I also observe nearly straight extinction in many of grains, which suggest lower variations in orientation within individual grains and lower defect densities. Taken together, the deformation microstructures developed at these temperatures are consistent with dislocation creep (i.e. dislocation glide and recovery). Recovery mechanisms include both recrystallization at grain boundaries as well as dislocation climb, leading to the formation of subgrain wails. The amount of recrystallization is greater than noted at lower temperatures for a given finite strain (Figure 10).

LPOs developed at these temperatures, are characterized by c-axis maxima parallel to the compression direction, consistent with c-, r-, and f-slip systems, continued reorientation by dislocation slip all of which may be accompanied by recovery processes (Figure 8). Increased recrystallization at high temperatures results in reductions in porphyroclast grain size and new, fine (< 5 μm) recrystallized grain sizes (Figure 9); thus, mean grain sizes are reduced significantly. Reductions in mean grain size is dependent on both temperature and degree of strain. Evidence for recovery and

recrystallization corresponds with the steady-state mechanical response of magnesite at these temperatures (Holyoke et al. (2014)). Differential stresses in samples deformed at T ≥800 ˚C increase initially, followed by yielding and reach nearly constant steady-stage values (~380-100 MPa) at low strains (Figure 3). The core-and-mantle microstructures are largely due to recrystallization at grain boundaries, but optically detected subgrains within grain interiors indicate that internal recovery and subgrain rotation are also important.

4.3 Grain size analysis

Grain sizes, excluding recrystallized grains, of samples deformed at 400-1000 ˚C were measured and mean values determined using two methods: determining the lengths of the long and short axes in the thin sections (ImageSXM) and finding their arithmetic mean, and measuring chord lengths along linear traverses then taking the arithmetic mean. The change in grain size with temperature is illustrated in Figure 9. The average grain size of samples deformed at low temperatures (400-700 ˚C) is similar to that of the undeformed starting material (~60 μm). At temperatures >750 ˚C, grain size decreases with increasing temperature and increasing strain. Unsurprisingly, this change in grain size coincides with the initiation of dynamic recrystallization.

Grain size distributions, excluding recrystallized grains, for samples deformed at temperatures of 400-1000 ˚C were calculated using Spektor's Chord analysis (Underwood (1970)) and the results for each sample are plotted in Figure 11 and Figure 12. As seen in Figure 11, the grain size distributions of samples deformed from 400-750

˚C are relatively similar to that of the undeformed sample. However, the distributions begin to shift to significantly smaller grain sizes at temperatures greater than 750 ˚C (Figure 12). As such, grain size distributions at these higher temperatures and higher strains yield size distributions with arithmetic means much smaller than the undeformed grain size distribution.

The average recrystallized grain size (Table 10) increased with increasing temperature; with the average grain size at 750 ˚C to be 1.9 μm (± 0.1 μm N = 50), at 800 ˚C to be 2.2 μm (± 0.1 μm N = 95), and at 900 ˚C to be 2.4 μm (± 0.1 μm N = 85). While these recrystallized grain sizes are similar to those observed by Stipp and Tullis (2003), steady-state deformation was never reached. As such, no recrystallized grain size piezometer was calculated.

The percentage of recrystallization (Figure 10) for each sample appears to depend on the total shortening strain and temperature of deformation. From 800 to 850 ˚C I observe a ~30% increase in recrystallized grains. However, from 850 ˚C to 900 ˚C I observe an increase in recrystallized grains of over a factor of 2.3. A comparison of the 900 ˚C and the 1000 ˚C shows that the percentage of recrystallized grains decreases, despite the increase in temperature. This decrease appears to be related to significant decrease in shortening (~ 18%) applied to the 1000 ˚C sample.

4.4 External rotations

In all of the polycrystalline magnesite samples, individual grains are constrained by surrounding grains or pistons at sample ends. Thus, dislocation slip, which causes

internal shear, combined with grain boundary constraints, leads to external rotations of the grain's crystallographic axes with respect to the direction of maximum compression. An external rotation, as defined by Sander (2013), is a rotation that occurs with respect to coordinates outside the deformed body. In the case of the experiments of Holyoke et al., 2014, the deforming lattice rotates such that the pole to an active glide plane rotates toward the direction of maximum compression. Such rotations can be observed for kink bands, relating the orientations of crystallographic axes within the deformed material of the kink band to the original crystallographic orientations of the host grain (Turner et al., 1954). The external rotations of a- and c-axes are related to the slip planes and directions and can, thus, be used to identify the operative slip systems. Rotations of c-axes within kink bands were determined by optical u-stage methods, but most slip system identification was facilitated by SEM EBSD measurements of a- and c-axes rotations.

4.5 Slip systems and mechanical twinning

Intracrystalline deformation by dislocation glide and mechanical twinning is restricted to shear on specific crystallographic planes in specific directions. In the case of dislocation slip, the plane and direction of shear define the slip system and in the case of mechanical twinning, the twin plane and twin glide direction characterize the strains due to twinning.

4.5.1 Slip systems

While the slip systems of calcite (Turner et al., 1954) and dolomite (Higgs and Handin, 1959; Barber and Wenk, 1979; Barber et al., 1981, Barber et al., 1983; Wenk and Zenger, 1983) have been characterized in numerous studies, none have yet to characterize the slip systems of magnesite. In this study, I made measurements of external rotations of crystallographic axes of well-defined kink bands using optical u-stage measurements and SEM EBSD measurements, and analyzed the results in terms of slip systems, following methods used by Turner et al., 1954 for calcite. Using the u-stage, orientations relative to the c-axis inside and outside of kink boundaries were collected to determine the misorientation of the band. These measurements were then used to infer slip systems. Unfortunately, kinked grains did not routinely exhibit cleavage cracks or deformation lamellae, therefore more classic methodologies to determine the specific slip-planes could not be used. However, using SEM EBSD, external rotations were identified by comparing the change in orientations of a- and c-axes within kink bands to those of the host grain. These measurements were then used to identify the specific rotation axis perpendicular to the slip direction in each kinked grain. Using the rotation axis and the degree of misorientation of the kink section from the host, a specific slip vector was identified.

Two classes of external rotation were identified using SEM EBSD data for kink bands. In the first case, the rotation axis corresponded to one of the a-axes. This implies that slip occurred perpendicular to the a-axis (Figure 13). Three possible slip systems of rhombohedral carbonates are possible based on this rotation axis: slip on e-, f-, or r-

planes, in the $\langle 40\bar{4}1\rangle, \langle\bar{1}01\bar{1}\rangle$, and $\langle\bar{2}021\rangle$ directions, respectively. In some cases, I was able to isolate the specific slip system. For the specific slip to be identified, grains had to be nearly perfectly oriented for slip along one of the aforementioned planes (Figure 14). In the second case, the rotation axis was in the basal plane of magnesite, at 30˚ from the a-axis as measured within the basal plane. In these cases, the only possible slip system for a rhombohedral carbonate is slip on the c-plane in the r- direction (Figure 15). Of the sharply defined kink bands analyzed, 12 are consistent with slip on r, f and c. At low temperatures (≤ 700 ˚C) I observed slip on the r-, f-, and c-axes. However, at higher temperatures (>700) slip was observed on only r- and f- axes.

4.5.2 Twinning

Optical analyses of samples deformed at 400 and 500 ˚C exhibit rare e- and f-twins. Based on the common mineral structures of calcite and magnesite, Johnsen, 1902 predicted that magnesite may exhibit twinning on the e-plane. However, we know of no reported observations of twins in magnesite. The role of e-twins in the deformation of calcite was investigated by Turner et al., 1954, and later by Jamison and Spang, 1976 and Rowe and Rutter, 1990. Mechanical twinning of dolomite on f-planes was investigated by Higgs and Handin (1959). In this study, I have observed both e- and f-twins of magnesite. The orientation of twin planes are 68˚ to <u>c</u> (for e-twinning) and 32˚ to <u>c</u> (for f-twinning) with twin glide directions of $< 40\bar{4}1 >$ (for e-twinning) and $< 0\bar{1}11 >$ (for f-twinning).

Samples deformed at T = 400, 500 ˚C reached differential stresses of 1120 and 930 MPa respectively. In these samples, most grains exhibit undulatory extinction and kink bands and only a small subset of grains exhibit mechanical twins. Given that twinning in magnesite has never been reported, I made careful measurements of twin boundary orientations relative to the c-axis and the compressive direction of σ_1 using the classic U-stage methods of Turner et al., 1954. Most mechanical twins were found to twin on *e* ($\{\bar{1}018\}$, $\{\bar{1}012\}$) (Figure 4a). However, 2 grains were identified to twin on *f* (Figure 16).

4.6 Lattice preferred orientations

Orientations of c- and a-axes of samples deformed at 400, 700, and 900 ˚C were collected from ~500 grains by SEM EBSD. The undeformed starting material exhibits a slight lattice-preferred orientation (Figure 5). Samples deformed at 400 ˚C, 700 ˚C, and 900 ˚C show a c-axis maxima roughly parallel to the maximum compressive direction. Unlike the c-axes, the a-axes exhibit little or no preferred orientations. The results of these analyses can be seen in Figure 6, Figure 7, and Figure 8.

5. DISCUSSION

5.1 Fabric strength

The lattice preferred orientations that develop due to dislocation slip depend on the external rotations of the active slip systems. A remarkable observation is that the c-axis maxima parallel to the compression direction is stronger at low temperatures (T = 400 and 700 ˚C) than that of the broad, lower concentration c-axis maxima measured for deformation at T = 900 ˚C. At higher temperatures, basal slip was not identified in our measurements and likely is very limited or does not occur at these temperatures. This is because slip on the basal plane results in external rotations of the c-axis towards σ_1 and therefore result in a tight fabric alignment to σ_1 on the c plane. Slip on the r and f planes results in the rotations of those planes toward σ_1. Slip on these planes produces a much wider spread of c-axis orientations relative to σ_1. As a result, I suspect that the more diffuse, lower concentration of c-axes parallel to σ_1 in the 900 ˚C sample comes as a result of diminished or absent basal slip.

5.2 Critically resolved shear stresses for mechanical twinning

Given that twins are extremely thin (less than optical resolution), measurement of external rotations of c-axes due to mechanical twinning by optical u-stage methods proved to be impossible. Twins were even challenging to investigate in SEM EBSD, with twin thickness < 0.2 μm. Thus, I relied on TEM diffraction data to detect the

crystallographic symmetry of the twins. The foil used for TEM analysis contained one potential twin and this twin was confirmed by double diffraction.

Following assumptions made by Jamison and Spang (1976), I assume that the local stress imposed on an individual grain that exhibits a twin is the same as the stress imposed on the entire sample. This assumption implies that stresses within the deforming aggregate are relatively homogenous. Given that this assumption is a good approximation, determination of critically resolved shear stress (CRSS) depends on the orientation of the twin plane to the stress direction, and the orientation of the twin plane direction relative to the maximum compression direction. The CRSS for twinning can be determined by Schmid's Law (Haase and Schmid, 1925):

$$\tau_c = S \cdot \Delta\sigma$$

where τ_c is the CRSS, $\Delta\sigma$ is the differential stress were S, the Schmid factor, is given by the equation

$$S = \cos\psi \cdot \cos\lambda$$

where Ψ is the angle between σ_1 and the normal to the twin glide plane and λ is angle between σ_1 and the slip direction (Figure 18). Ψ can be determined within 2˚ and I have been able to constrain λ within 3˚. Thus, Schmid factors were determined (Table 2). In all cases, Schmid factors were large. This implies that twin gliding requires large CRSS, and that stresses imposed on the magnesite samples was just large enough to activate twin gliding in grains that are optimally oriented for twin glide.

In contrast to the few grains in magnesite, samples that exhibit twinning in deformed calcite aggregates contain large populations of twinned grains and CRSS

values of these twins is small (Figure 19). Samples of deformed dolomite contain significantly lower twin densities that that of calcite. However, even these diminished twin densities are significantly greater than observed in the deformed magnesite samples. In addition, CRSS values of dolomite twins (Figure 19) are significantly greater than that of calcite. However, in comparison to the CRSS values of magnesite twins (Figure 19), dolomite twin CRSS values are also quite small. Figure 19 compares the CRSS of e- and f- twins for calcite, dolomite, and magnesite at 400 and 500 ˚C. The CRSS of magnesite twins (324-514 MPa) is significantly greater than that of both calcite and dolomite. Previous studies (Barber, 1977, Barber et al., 1981; Barber and Wenk, 2001; Davis et al., 2008) attributed the CRSS strength differences between calcite and dolomite to differences in their crystal symmetry and to cation ordering in dolomite. However, with the addition of magnesite CRSS values, neither theory holds true. This led me to reevaluate the factors controlling CRSS in rhombohedral carbonate.

5.3 Effects of cation size on strength and anion repulsion

Early comparisons between mechanical properties and the CRSS of calcite and dolomite led to the hypothesis that cation ordering in dolomite may be responsible for its strength by dislocation processes and twinning. More recently however, (Holyoke et al., 2014) showed that magnesite is stronger than dolomite over a wide range of conditions (despite the fact that it shares the same structure and symmetry with calcite). Comparisons of the mechanical data for calcite, dolomite, and magnesite show that increasing strengths correspond to increasing Mg contents. This trend is further

corroborated by CRSS strength trends, which again indicates that strength corresponds to magnesium content. One significant difference between calcium and magnesium cations is their ionic radii. In calcite, dolomite, and magnesite, bulk cation sizes (Ca^{2+}, Ca^{2+} and Mg^{2+}, Mg^{2+}) differ while anion sizes (CO_3^{2-}) remain constant. With this in mind, I developed a conceptual model that provides an explanation for the mechanical trends observed. This model is based on what we know about twinning in calcite and variations in bond length, as modeled by Bruno et al., 2010.

5.4 Calcite O-O distances across twin boundaries

A recent *ab initio* modeling study by Bruno et al., 2010 modeled the elastically strained crystal lattice of calcite around a twin plane for each of the four possible twin laws. The model allows the structure of calcite surrounding a twin to relax to the lowest possible energy state. Bruno et al., 2010 reported that C-O bond distance near twin boundaries remained almost unchanged. However, Ca-O bond distances changed quite significantly near the twin planes. For instance, Ca-O distances for e-twins varied (2.339 - 2.4106 Å) significantly near twin boundaries when compared to the unstrained lattice (2.368 Å). Unfortunately, they did not measure O-O distances across the twin planes. Fortunately, they provided me their model and I was able to measure O-O distances. Using the results of their *ab initio* twin models, I measured the O-O anion distances directly across the twin plane and found that the two closest O-O anion distances were abnormally close to one another. For example, the closest O-O anion distance directly across a twin boundary for a calcite f-twin was 2.901 Å and the unstrained lattice 3.16 Å.

This is `10% difference in O-O distance in calcite f-twins. With smaller unit cells, (i.e. smaller cation sizes) the O-O distances are expected to be even closer. Therefore, the repulsive forces between these closest two O-O anions will be larger, supporting the idea that cation size controls the strength of mechanical twinning and dislocation movement.

Given that we do not know the structures of dislocation cores in carbonates, I examine the potential effects of cation slip and CO_3 interferences on mechanical twinning to demonstrate how cationic size influences strength of crystal-plastic deformation. Figure 21a and Figure 21b show the proposed structures of e- and f-twins of magnesite based on *ab initio* calculations of e- and f-twins for calcite. Given the smaller size of Mg^{2+}, CO_3^{-2} groups across twin boundaries are required to become closer in magnesite than in calcite. Magnesium, with its smaller cationic radius and therefore a smaller unit cell, forces opposing CO_3^{2-} anions across a twin boundary closer together than that of calcium. Thus, mechanical twins in magnesite will need to overcome larger anion-anion repulsion. By this model, magnesite is expected to require a greater twin CRSS (due to the larger repulsive forces) than calcite or dolomite.

While we do not know the structures of dislocation cores, we do know that the motion of dislocations requires elastic distortions of the lattice. These elastic distortions, like in mechanical twinning, cause anions to be forced closer to one another. Therefore, I infer that the higher CRSS values for slip in magnesite, in comparison to other rhombohedral carbonates (Holyoke et al., 2014), comes as a result of increased Mg content. Additionally, Holyoke et al., 2014 discussed how the large elastic modulus of magnesite might explain why high inelastic strengths are observed. Anion-anion

repulsion, and therefore the size of the anions contained in the lattice, may significantly influence the elastic strength of the Ca-Mg rhombohedral carbonates.

5.5 Potential importance of cation sizes and anion repulsions in other minerals

The influence of cationic size on mechanical twinning and dislocation slip strengths may not be limited to just carbonates, and may explain variations in critically resolved shear stresses and dislocation glide in other minerals. For example, r-twins can be created under shear stresses for both hematite and corundum, which have the same crystal structures with cation sites occupied by Fe^{3+} in hematite and by Al^{3+} in corundum. Fe^{3+} and Al^{3+} in octahedral coordination sites have ionic radii of 78.5 Å and 67.5 Å respectively. The CRSS of r-twins of these two minerals differs vastly from one another (Figure 22) and corundum, with the smaller cation shows a significantly stronger CRSS value. Another example of this effect can be observed when comparing the high-temperature rheologies of olivine single-crystals of differing fayolite (the Fe end-member) and forsterite (the Mg end-member) contents (Figure 23). The ionic radii of Fe^{2+} and Mg^{2+} in octahedral coordination sites have ionic radii of 92 Å and 86 Å respectively. Following the trend of the Mg-Ca carbonate system and Fe-Al oxide system, the samples deformed with larger concentrations of Mg^{2+} (the smaller cation), showed greater mechanical strengths. With this trend being observed in carbonates, oxides, and olivine groups it seems likely that cationic size affects twinning and dislocation slip strengths across all mineral groups.

6. CONCLUSIONS

Deformation microstructures of magnesite aggregates (grain size ~50 μm) deformed at an effective of 900 MPa, temperatures T = 400-1000 ˚C, and strain rates $\dot{\varepsilon} = 10^{-7} - 10^{-4}\ s^{-1}$ suggest changes in deformation mechanisms with increasing temperature. Samples of were subdivided into groups based on observed microstructures and inferred deformation mechanisms. At temperatures of 400 and 500 ˚C, many grains exhibit undulatory extinction and kink bands occur commonly. Mechanical twins, though rare, are observed at these temperatures. At temperatures of 600-750 ˚C, deformation appears more distributed; with most grains exhibiting undulatory extinction and kink bands occur frequently. Additionally, mechanical twins are no longer observed. At temperatures of 800-1000 ˚C, bulge recrystallized grains, subgrain rotation recrystallized grains, subgrains, and core-and-mantle structures are observed. In addition, grains show much more sweeping extinction patterns than samples at lower temperatures.

The microstructures observed at low temperatures (400-500˚C) indicate that multiple deformation mechanisms are active. The primary mechanism is dislocation glide, which is inferred by the abundance of kink bands within grains and grains exhibiting undulatory extinction. Twinning is the secondary deformation mechanism that is operative. Due to the scarcity of these mechanical twins, in conjunction with the very limited amount of strain that they can accommodate, I infer that mechanical twinning accommodated a trivial amount of deformation. Therefore, the dominant deformation

mechanism at these temperatures was dislocation glide. The microstructures observed at intermediate temperatures (600-750˚C) indicate that deformation was solely being accommodated by dislocation glide. At temperatures >750˚C, the abundance of recrystallized grains is indicative of dislocation glide operating in conjunction with climb recovery mechanisms.

There is strong microstructural relation to the rheology observed by Holyoke et al. (2014). At temperatures < 600 ˚C, Holyoke et al. (2014) reported a rheology consistent with low temperature crystal plasticity. This is corroborated by the dislocation glide microstructures described above. At temperatures ≥ 800 ˚C, Holyoke et al., 2014 reported a rheology primarily deforming by dislocation creep. The abundance of recrystallized grains, core-and-mantle structures, and subgrains is in agreement with the mechanical response reported. This strong agreement between the mechanical and microstructural studies is likely due to the dominance of a single deformation mechanism operating at each experimental temperature.

Magnesite slips on r-, f-, and c- planes and twins on e- and f-planes. The CRSS for both twin types in magnesite was found to exceed 300 MPa for all measurements. These CRSS values are significantly greater than those reported for e- and f-twins in calcite and dolomite. CRSS values in the rhombohedral carbonates systemically increase with increasing magnesium content. This strength trend corresponds with increasing volumes of smaller cations.

Increasing cation size in mineral systems containing differing cations corresponds to a decrease in force required to generate twins or cause dislocations to slip. These results

are observed in the carbonate system analyzed in this study, in a comparison of oxides, and in the comparison of the olivine end-members.

This cation size influence on the mechanical strength of twinning and slip may result from anion-anion repulsion directly around the crystal-plastic perturbation. This appears to be corroborated by an ab *initio* study of calcite twins by Bruno et al., 2010. Their data indicates that O-O distances proximal to twin boundaries are significantly closer to one another than in the unstrained crystal lattice.

REFERENCES

Barber and Wenk, H.-R. (2001) Slip and dislocation behaviour in dolomite. European Journal of Mineralogy 13, 221-243.

Barber, D. (1977) Defect microstructures in deformed and recovered dolomites. Tectonophysics 39, 193-213.

Barber, D., Freeman, L. and Smith, D.J. (1983) Analysis of high-voltage, high-resolution images of lattice defects in experimentally-deformed dolomite. Physics and Chemistry of Minerals 9, 102-108.

Barber, D., Heard, H. and Wenk, H. (1981) Deformation of dolomite single crystals from 20–800 C. Physics and Chemistry of Minerals 7, 271-286.

Barber, D. and Wenk, H. (1979) On geological aspects of calcite microstructure. Tectonophysics 54, 45-60.

Barber, D.J., Wenk, H.-R. and Heard, H.C. (1994) The plastic deformation of polycrystalline dolomite: comparison of experimental results with theoretical predictions. Materials Science and Engineering: A 175, 83-104.

Bashir, E., Naseem, S., Akhtar, T. and Shireen, K. (2009) Characteristics of ultramafic rocks and associated magnesite deposits, Nal Area, Khuzdar, Balochistan, Pakistan. Journal of Geology and Mining Research 1, 034-041.

Biellmann, C., Gillet, P., Peyronneau, J. and Reynard, B. (1993) Experimental evidence for carbonate stability in the Earth's lower mantle. Earth and Planetary Science Letters 118, 31-41.

Billi, A. and Di Toro, G. (2008) Fault-related carbonate rocks and earthquake indicators: recent advances and future trends. Structural Geology: New Research, 63-86.

Borg, I. and Handin, J. (1967) Torsion of calcite single crystals. Journal of Geophysical Research 72, 641-669.

Borg, I. and Turner, F.J. (1953) Deformation of Yule Marble: Part VI—Identity and Significance of Deformation Lamellae and Partings in Calcite Grains. Geological Society of America Bulletin 64, 1343-1352.

Braillon, P., Kubin, L. and Serughetti, J. (1978) Plastic deformation of calcite single crystals deformed in compression parallel to [111]. physica status solidi (a) 45, 453-462.

Braillon, P. and Serughetti, J. (1976) Déformation plastique de monocristaux de calcite en compression suivant 〈001〉. physica status solidi (a) 36, 637-646.

Bresser, D., Ter Heege, J. and Spiers, C. (2001) Grain size reduction by dynamic recrystallization: can it result in major rheological weakening? International Journal of Earth Sciences 90, 28-45.

Bruno, M., Massaro, F.R., Rubbo, M., Prencipe, M. and Aquilano, D. (2010) (10.4),(01.8),(01.2), and (00.1) Twin Laws of Calcite (CaCO3): Equilibrium Geometry of the Twin Boundary Interfaces and Twinning Energy. Crystal Growth & Design 10, 3102-3109.

Burkhard, M. (1993) Calcite twins, their geometry, appearance and significance as stress-strain markers and indicators of tectonic regime: a review. Journal of Structural Geology 15, 351-368.

Busch, J.P. and Van der Pluijm, B.A. (1995) Calcite textures, microstructures and rheological properties of marble mylonites in the Bancroft shear zone, Ontario, Canada. Journal of Structural Geology 17, 677-688.

Casey, M., Kunze, K. and Olgaard, D.L. (1998) Texture of Solnhofen limestone deformed to high strains in torsion. Journal of Structural Geology 20, 255-267.

Davis, N., Kronenberg, A. and Newman, J. (2008) Plasticity and diffusion creep of dolomite. Tectonophysics 456, 127-146.

Davis, N., Newman, J., Wheelock, P. and Kronenberg, A. (2011) Grain growth kinetics of dolomite, magnesite and calcite: a comparative study. Physics and Chemistry of Minerals 38, 123-138.

De Bresser, J. (2002) On the mechanism of dislocation creep of calcite at high temperature: inferences from experimentally measured pressure sensitivity and strain rate sensitivity of flow stress. Journal of Geophysical Research: Solid Earth (1978–2012) 107, ECV 4-1-ECV 4-16.

De Bresser, J. and Spiers, C. (1990) High-temperature deformation of calcite single crystals by r+ and f+ slip. Geological Society, London, Special Publications 54, 285-298.

De Bresser, J. and Spiers, C. (1993) Slip systems in calcite single crystals deformed at 300–800 C. Journal of Geophysical Research: Solid Earth (1978–2012) 98, 6397-6409.

De Bresser, J., Urai, J. and Olgaard, D. (2005) Effect of water on the strength and microstructure of Carrara marble axially compressed at high temperature. Journal of Structural Geology 27, 265-281.

Delle Piane, C., Burlini, L., Kunze, K., Brack, P. and Burg, J.P. (2008) Rheology of dolomite: large strain torsion experiments and natural examples. Journal of Structural Geology 30, 767-776.

Dobrzhinetskaya, L.F., Wirth, R. and Green, H.W. (2006) Nanometric inclusions of carbonates in Kokchetav diamonds from Kazakhstan: A new constraint for the depth of metamorphic diamond crystallization. Earth and Planetary Science Letters 243, 85-93.

Fairbairn, H.W. and Hawkes, H.E. (1941) Dolomite orientation in deformed rocks. American Journal of Science 239, 617-632.

Ferrill, D.A., Morris, A.P., Evans, M.A., Burkhard, M., Groshong, R.H. and Onasch, C.M. (2004) Calcite twin morphology: a low-temperature deformation geothermometer. Journal of Structural Geology 26, 1521-1529.

Fondriest, M., Smith, S.A., Di Toro, G., Zampieri, D. and Mittempergher, S. (2012) Fault zone structure and seismic slip localization in dolostones, an example from the Southern Alps, Italy. Journal of structural Geology 45, 52-67.

Fredrich, J.T., Evans, B. and Wong, T.F. (1989) Micromechanics of the brittle to plastic transition in Carrara marble. Journal of Geophysical Research: Solid Earth (1978–2012) 94, 4129-4145.

Gillet, P. (1993) Stability Of Magnesite (MgCO3) At Mantle Pressure And Temperature Conditions-A Raman-Spectroscopic Study. American Mineralogist 78, 1328-1331.

Goldsmith, J.R., Graf, D.L. and Joensuu, O.I. (1955) The occurrence of magnesian calcites in nature. Geochimica et Cosmochimica Acta 7, 212-230.

Griggs, D. and Miller, W. (1951) Deformation of Yule marble: part I—compression and extension experiments on dry Yule marble at 10,000 atmospheres confining pressure, room temperature. Geological Society of America Bulletin 62, 853-862.

Griggs, D., Turner, F.J., Borg, I. and Sosoka, J. (1951) Deformation of Yule Marble: Part IV—Effects at 150° C. Geological Society of America Bulletin 62, 1385-1406.

Griggs, D., Turner, F.J., Borg, I. and Sosoka, J. (1953) Deformation of Yule marble: Part V—Effects at 300° C. Geological Society of America Bulletin 64, 1327-1342.

Griggs, D.T., Turner, F. and Heard, H. (1960) Deformation of Rocks at 500° to 800° C. Geological Society of America Memoirs 79, 39-104.

Groshong, R. (1972) Strain calculated from twinning in calcite. Geological Society of America Bulletin 83, 2025-2038.

Haase, O. and Schmid, E. (1925) Über den Gleitwiderstand von Metallkristallen. Zeitschrift für Physik 33, 413-428.

Handin, J. and Hager Jr, R.V. (1957) Experimental deformation of sedimentary rocks under confining pressure: tests at room temperature on dry samples. AAPG Bulletin 41, 1-50.

Handin, J.W. and Griggs, D. (1951) Deformation of Yule marble: Part II—predicted fabric changes. Geological Society of America Bulletin 62, 863-886.

Heard, H. (1976) Comparison of the flow properties of rocks at crustal conditions. Philosophical Transactions of the Royal Society of London A: Mathematical, Physical and Engineering Sciences 283, 173-186.

Heard, H. and Raleigh, C. (1972) Steady-state flow in marble at 500 to 800 C. Geological Society of America Bulletin 83, 935-956.

Herwegh, M., De Bresser, J. and Ter Heege, J. (2005) Combining natural microstructures with composite flow laws: an improved approach for the extrapolation of lab data to nature. Journal of Structural Geology 27, 503-521.

Higgs, D.V. and Handin, J. (1959) Experimental deformation of dolomite single crystals. Geological Society of America Bulletin 70, 245-278.

Hirth, G. and Tullis, J. (1992) Dislocation creep regimes in quartz aggregates. Journal of Structural Geology 14, 145-159.

Holyoke, C., Kronenberg, A., Newman, J. and Ulrich, C. (2013) Rheology of magnesite and implications for subduction zone dynamics, AGU Fall Meeting Abstracts, p. 02.

Holyoke, C.W., Kronenberg, A.K., Newman, J. and Ulrich, C. (2014) Rheology of magnesite. Journal of Geophysical Research: Solid Earth 119, 6534-6557.

Holyoke, C.W. and Tullis, J. (2006) Mechanisms of weak phase interconnection and the effects of phase strength contrast on fabric development. Journal of Structural Geology 28, 621-640.

House, W.M. and Gray, D.R. (1982) Cataclasites along the Saltville thrust, USA and their implications for thrust-sheet emplacement. Journal of Structural Geology 4, 257-269.

Ibarguchi, G. (1999) Deformation, high-pressure metamorphism and exhumation of ultramafic rocks in a deep subduction/collision setting (Cabo Ortegal, NW Spain). Journal of Metamorphic Geology 17, 747-764.

Jamison, W.R. and Spang, J.H. (1976) Use of calcite twin lamellae to infer differential stress. Geological Society of America Bulletin 87, 868-872.

Johnsen, A. (1902) Biegungen und Translationen. N Jb Mineral Geol Palaeontol, 133-153.

Kerrick, D. and Connolly, J. (2001) Metamorphic devolatilization of subducted oceanic metabasalts: implications for seismicity, arc magmatism and volatile recycling. Earth and Planetary Science Letters 189, 19-29.

Kushiro, I. (1975) Carbonate-silicate reactions at high presures and possible presence of dolomite and magnesite in the upper mantle. Earth and Planetary Science Letters 28, 116-120.

Neumann, E.-R. (1969) Experimental recrystallization of dolomite and comparison of preferred orientations of calcite and dolomite in deformed rocks. The Journal of Geology, 426-438.

Newman, J. and Mitra, G. (1993) Lateral variations in mylonite zone thickness as influenced by fluid-rock interactions, Linville Falls fault, North Carolina. Journal of Structural Geology 15, 849-863.

Paterson, M. and Olgaard, D. (2000) Rock deformation tests to large shear strains in torsion. Journal of Structural Geology 22, 1341-1358.

Paterson, M. and Turner, F. (1970) Experimental deformation of constrained crystals of calcite in extension, Experimental and Natural Rock Deformation/Experimentelle und natürliche Gesteinsverformung. Springer, pp. 109-141.

Pieri, M., Kunze, K., Burlini, L., Stretton, I., Olgaard, D., Burg, J.-P. and Wenk, H.-R. (2001) Texture development of calcite by deformation and dynamic recrystallization at 1000K during torsion experiments of marble to large strains. Tectonophysics 330, 119-140.

Plank, T. and Langmuir, C.H. (1998) The chemical composition of subducting sediment and its consequences for the crust and mantle. Chemical geology 145, 325-394.

Renner, J., Evans, B. and Siddiqi, G. (2002) Dislocation creep of calcite. Journal of Geophysical Research: Solid Earth (1978–2012) 107, ECV 6-1-ECV 6-16.

Rowe, K. and Rutter, E. (1990) Palaeostress estimation using calcite twinning: experimental calibration and application to nature. Journal of Structural Geology 12, 1-17.

Rutter, E. and Elliott, D. (1976) The kinetics of rock deformation by pressure solution [and discussion]. Philosophical Transactions of the Royal Society of London A: Mathematical, Physical and Engineering Sciences 283, 203-219.

Rybacki, E., Paterson, M.S., Wirth, R. and Dresen, G. (2003) Rheology of calcite–quartz aggregates deformed to large strain in torsion. Journal of Geophysical Research: Solid Earth (1978–2012) 108.

Sander, B. (2013) Einführung in die Gefügekunde der Geologischen Körper: Zweiter Teil Die Korngefüge. Springer-Verlag.

Sasvári, T. and Kondela, J. (2007) Demonstration of Alpine structural phenomena at the structure of magnesite deposit Jelšava-Dúbrava Massif. Metalurgija 46, 117-122.

Sato, K. and Katsura, T. (2001) Experimental investigation on dolomite dissociation into aragonite+ magnesite up to 8.5 GPa. Earth and Planetary Science Letters 184, 529-534.

Schmid, S. (1976) Rheological evidence for changes in the deformation mechanism of Solenhofen limestone towards low stresses. Tectonophysics 31, T21-T28.

Schmid, S., Panozzo, R. and Bauer, S. (1987) Simple shear experiments on calcite rocks: rheology and microfabric. Journal of structural Geology 9, 747-778.

Schmid, S., Paterson, M. and Boland, J. (1980) High temperature flow and dynamic recrystallization in Carrara marble. Tectonophysics 65, 245-280.

Stipp, M. and Tullis, J. (2003) The recrystallized grain size piezometer for quartz. Geophysical Research Letters 30.

Thomas, J. and Renshaw, G. (1967) Influence of dislocations on the thermal decomposition of calcium carbonate. Journal of the Chemical Society A: Inorganic, Physical, Theoretical, 2058-2061.

Tullis, J. and Yund, R.A. (1985) Dynamic recrystallization of feldspar: a mechanism for ductile shear zone formation. Geology 13, 238-241.

Turner, F. and Heard, H. (1965) Deformation in calcite crystals at different strain rates. University of California Publications in Geological Sciences 46, 103-126.

Turner, F.J. and Ch'ih, C. (1951) Deformation of Yule marble: Part III—Observed fabric changes due to deformation at 10,000 atmospheres confining pressure, room temperature, dry. Geological Society of America Bulletin 62, 887-906.

Turner, F.J. and Orozco, M. (1976) Crystal bending in metamorphic calcite, and its relations to associated twinning. Contributions to Mineralogy and Petrology 57, 83-97.

Turner, F.J., T Griggs, D., Clark, R. and Dixon, R.H. (1956) Deformation of Yule marble. Part VII: Development of oriented fabrics at 300° C–500° C. Geological Society of America Bulletin 67, 1259-1294.

Turner, F.J., T Griggs, D. and Heard, H. (1954) Experimental deformation of calcite crystals. Geological Society of America Bulletin 65, 883-934.

Twiss, R.J. (1977) Theory and applicability of a recrystallized grain size paleopiezometer, Stress in the Earth. Springer, pp. 227-244.

Underwood, E.E. (1970) Quantitative stereology.

Wada, H., Tomita, T., Matsuura, K., Tuchi, K., Ito, M. and Morikiyo, T. (1994) Graphitization of carbonaceous matter during metamorphism with references to carbonate and pelitic rocks of contact and regional metamorphisms, Japan. Contributions to Mineralogy and Petrology 118, 217-228.

Wang, Z.C., Bai, Q., Dresen, G., Wirth, R. and Evans, B. (1996) High-temperature deformation of calcite single crystals. Journal of Geophysical Research: Solid Earth (1978–2012) 101, 20377-20390.

Weiss, L. and Turner, F. (1972) Some observations on translation gliding and kinking in experimentally deformed calcite and dolomite. Flow and Fracture of Rocks, 95-107.

Wenk, H. and Zenger, D. (1983) Sequential basal faults in Devonian dolomite, Nopah Range, Death Valley area, California. Science 222, 502-504.

Zhu, Y. and Ogasawara, Y. (2002) Phlogopite and coesite exsolution from super-silicic clinopyroxene. International Geology Review 44, 831-836.

APPENDIX

TABLES

Table 1: List of all experiments

Experiment	Assembly	Temperature (Davis et al.)	Confining pressure[1] (MPa)	Strain rate (s^{-1})	Strain (%)	Peak strength[2,3] (MPa)	Final strength[3] (MPa)
Single Deformation Step Experiments							
M-14	SSA[5]	400	900	$1.6*10^{-5}$	10	1120	1120
M-13	SSA	600	925	$1.6*10^{-5}$	18	725	725
M-11	SSA	700	950	$1.6*10^{-5}$	28	470	420
M-27	SSA	750	1100	$1.6*10^{-5}$	23	312	296.8
M-10	SSA	800	1050	$1.6*10^{-5}$	28	230	220
M-28	SSA	850	1100	$1.6*10^{-5}$	28	249	151.5
M-24	SSA	900	1170	$1.6*10^{-5}$	28	253	152
M-17	MSA[4]	1000	1625	$1.6*10^{-5}$	16	30	10
Strain Rate-Stepping Experiments							
M-21		500	1000	$1.6*10^{-7}$	9	670	670
				$1.6*10^{-6}$	4	850	850
				$1.6*10^{-5}$	4	1050	1050
				$1.6*10^{-4}$	4	1250	1250

[1] – P_{eff} = 900 MPa for all experiments
[2] – Strain in parentheses, if different than final strain
[3] – Corrected using methods described in Holyoke and Kronenberg (2010)
[4] – Molten salt assembly
[5] – Solid salt assembly

Table 2: CRSS values for magnesite e- and f-twins

θ from C	φ	λ_1	λ_2	S_{max}	S_{min}	CRSS (MPa)	σ_{Peak} (Mpa)
M-14	**400 ˚C**						
e-twin:							
86	46	44	55	0.49	0.39	436	1118
77	42	50	56	0.48	0.42	470	
74	56	34	47	0.46	0.38	425	
74	68	23	30	0.34	0.32	358	
70	47	124	128	0.41	0.38	425	
69	60	34	44	0.41	0.35	391	
69	60	30	37	0.43	0.40	447	
68	57	56	37	0.43	0.30	335	
68	64	48	29	0.38	0.29	324	
67	56	49	34	0.46	0.36	402	
66	38	58	52	0.48	0.41	458	
66	46	52	44	0.49	0.42	470	
66	46	48	44	0.49	0.46	514	
64	54	48	46	0.40	0.39	436	
63	50	44	40	0.49	0.46	514	
63	38	54	50	0.49	0.46	514	
62	48	50	42	0.49	0.43	481	
62	68	27	24	0.34	0.33	369	
62	50	57	39	0.49	0.35	391	
62	65	30	26	0.38	0.37	414	
f-twin							
37	35	61	55	0.46	0.39	436	
M-21	**500 ˚C**						
e-twin							
67	43	124	132	0.49	0.41	380	928

Table 3: Kink band slip systems identified

Temperature (˚C)	c-slip	r+-slip	f+-slip	r-,f-slip
400	2	0	0	0
500	0	1	1	0
600	0	0	2	0
700	3	0	0	1
800	0	0	0	2
900	0	0	0	1
Total	5	1	3	4

Table 4: Calcite twin glide and slip systems

Experimental conditions	Temperature (Davis et al.)	Strain rate (s^{-1})	Pressure (MPa)	Reference
Twinning systems:				
$e^{+}\{\bar{1}018\}\langle 40\bar{4}1\rangle$	20-300	2.5×10^{-4}	500-1000	Turner et al. (1954)
	300-800	2.5×10^{-4}	500	Griggs et al. (1960)
$r^{+}\{10\bar{1}4\}\langle\bar{2}021\rangle$	20	torsion tests	300	Borg and Handin (1967)
	300	?	500	Weiss and Turner (1972)
$f^{-}\{\bar{1}012\}\langle\bar{1}01\bar{1}\rangle$	300?	?	500	Paterson and Turner (1970)
Slip Systems:				
$r^{-}\{10\bar{1}4\}\langle 20\bar{2}\bar{1}\rangle$	20-400	2.5×10^{-4}	300-1000	Turner et al. (1954)
	300-600	2.5×10^{-4}	500	Griggs et al. (1960)
	25-500	4×10^{-1}, 3×10^{-7}	500	Turner and Heard (1965)
	300-800	3×10^{-5}	Unconf.	De Bresser and Spiers (1990)
$r^{+}\{10\bar{1}4\}\langle\bar{2}021\rangle$	300	?	500	Weiss and Turner (1972)
	460-550	1×10^{-4}	Unconf.	Braillon and Serughetti (1976)
	350-650	2.5×10^{-8}	Unconf.	Barber and Wenk (1979)
	550-800	$3 \times 10^{-4} - 3 \times 10^{-8}$	Unconf.	De Bresser and Spiers (1990)
$f^{-}\{\bar{1}012\}\langle\bar{2}20\bar{1}\rangle\langle 0\bar{2}2\bar{1}\rangle$	20, (300?)	2.5×10^{-4}	500	Turner et al. (1954)
		2.5×10^{-4}	500	Griggs et al. (1960)
$f^{+}\{\bar{1}012\}\langle\bar{2}20\bar{1}\rangle\langle 0\bar{2}2\bar{1}\rangle$	575-650	2.5×10^{-5}	Unconf.	De Bresser and Spiers (1990)
$f\{\bar{1}012\}\langle\bar{1}01\bar{1}\rangle$	600-800	2.5×10^{-5}	Unconf.	De Bresser and Spiers (1990)
$f^{+}\{\bar{1}012\}\langle 10\bar{1}1\rangle$	550-800	$3 \times 10^{-4} - 3 \times 10^{-8}$	Unconf.	De Bresser and Spiers (1990)
$f^{+}\{0001\}\langle\bar{1}2\bar{1}0\rangle$	800	2.5×10^{-4}	500	Griggs et al. (1960)
	300	2.5×10^{-4}	500	Turner and Orozco (1976)
	600-800	3×10^{-5}	Unconf.	De Bresser and Spiers (1993)
$a\{\bar{1}2\bar{1}0\}\langle\bar{2}021\rangle$	300, 500	?	500	Paterson and Turner (1970)
	300	3.3×10^{-7}	500	Turner and Heard (1965)
$m\{10\bar{1}0\}\langle\bar{1}2\bar{1}0\rangle$	550	?	?	Thomas and Renshaw (1967)

*Modified from De Bresser, 2002

Table 5: Dolomite twin glide and slip systems

Experimental conditions	Temperature (Davis et al.)	Strain rate (s^{-1})	Pressure (MPa)	Reference
Twinning systems:				
f-$\{01\bar{1}2\}\langle 0\bar{1}11\rangle$	380	?	304	Turner et al. (1954)
	300-600	1.3×10^{-5}	100-415	Barber et al. (1981)
Slip Systems:				
c-$\{0001\}\langle 11\bar{2}0\rangle$	?	?	?	Johnsen (1902)
	300-420	?	?	Barber and Wenk (2001)
	300-600	1.3×10^{-5}	100-415	Barber et al. (1981)
f-$\{\bar{1}012\}\langle\bar{2}20\bar{1}\rangle$	?	natural	?	Fairbairn and Hawkes (1941)
	300-600	1.3×10^{-5}	100-415	Barber et al. (1981)
	300-420	?	?	Barber and Wenk (2001)
r+$\{\bar{1}012\}\langle 11\bar{2}0\rangle$	300-420	?	?	Barber and Wenk (2001)
	550-800	$3 \times 10^{-4} - 3 \times 10^{-8}$	Unconf.	De Bresser and Spiers (1990)

Table 6: Magnesite twin glide and slip systems

Experimental conditions	Temperature (Davis et al.)	Strain rate (s^{-1})	Pressure (MPa)	Reference
Twinning systems:				
Slip Systems:				
c{0001}	?	?	?	Johnsen (1902) (predicted but not observed)

Table 7: Magnesite twin laws and slip systems identified from this study

Experimental conditions	Temperature (Davis et al.)	Strain rate (s^{-1})	Pressure (MPa)	Reference
Twinning systems:				
$e^{+}\{\bar{1}018\}\langle 40\bar{4}1\rangle$	400-500	$1.6*10^{-5}$	900	
$f^{+}\{\bar{1}012\}\langle 10\bar{1}1\rangle$	400-500	$1.6*10^{-5}$	900	
Slip Systems:				
$c^{-}\{0001\}\langle 11\bar{2}0\rangle$	400-650	$1.6*10^{-5}$	900-1100	
$f^{+}\{\bar{1}012\}\langle 10\bar{1}1\rangle$	400-1000	$1.6*10^{-5}$	900-1100	
$r+\{\bar{1}012\}\langle 11\bar{2}0\rangle$	400-1000	$1.6*10^{-5}$	900-1100	

Table 8: Crystallographic dimensions of calcite, dolomite, and magnesite

Name	Formula	Specific gravity (g/cm^3)	Cell dimensions (Å)	
			a	***c***
Calcite	$CaCO_3$	2.71	4.989	17.061
Dolomite	$CaMg(CO_3)_2$	2.85	4.807	16.003
Magnesite	$MgCO_3$	3.00	4.632	15.012

Table 9: Results of ImageSXM grain shape analysis

Experiment	Temperature (Davis et al.)	Strain rate (s^{-1})	Strain (%)	Long Axis (µm)	Short Axis (µm)	Axial Ratio
Undeformed Nevada Magnesite						
M-0	n/a	n/a	n/a	68.97	37.69	1.83
Single Deformation Step Experiments						
M-14	400	$1.6*10^{-5}$	10	71.10	33.07	2.15
M-13	600	$1.6*10^{-5}$	18	71.90	40.98	1.75
M-11	700	$1.6*10^{-5}$	28	64.61	32.61	1.98
M-27	750	$1.6*10^{-5}$	23	57.51	31.18	1.84
M-10	800	$1.6*10^{-5}$	28	38.79	18.27	2.12
M-28	850	$1.6*10^{-5}$	28	25.98	12.39	2.10
M-24	900	$1.6*10^{-5}$	28	13.95	6.51	2.14
M-17	1000	$1.6*10^{-5}$	16	23.66	12.47	1.90
Strain Rate-Stepping Experiments						
M-21	500	$1.6*10^{-7}$	9	71.28	35.68	1.99
		$1.6*10^{-6}$	4			
		$1.6*10^{-5}$	4			
		$1.6*10^{-4}$	4			

Table 10: Recrystallized Grain Size by Temperature

Sample Number	Temperature (°C)	Mean Grain Size (μm)	Standard Deviation(μm)	N (# of grains)
M-17	750	1.89	0.61	50
M-10	800	2.19	0.76	95
M-24	900	2.44	0.99	85
M-17	1000	2.47	1.02	100

FIGURES

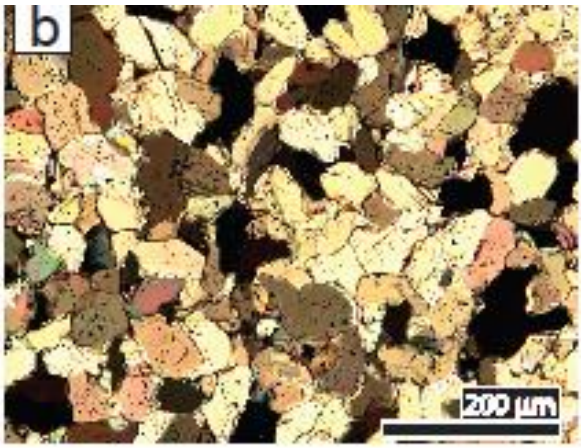

Figure 1: Photomicrograph of undeformed magnesite. Samples are from Nevada, USA, has an average grain size of ~60 µm , very low porosity (<1%), and rare inclusions (<<1%) of ultramafic or altered ultramafic materials. Grains are equant, exhibit straight extinction between crossed polarizers, and are free of twins.

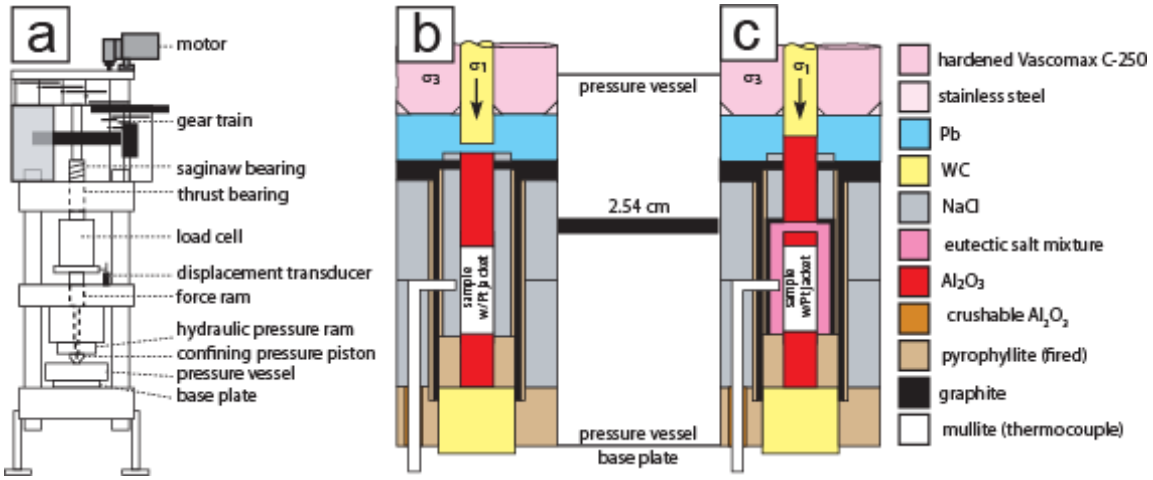

Figure 2: (a) schematic of a Griggs-type piston cylinder rock deformation apparatus, which has an external load cell (b) solid alt assembly used for experiments defomred from 400-900 ˚C (c) molten salt assembly used in experiments deformed at tempeatures > 900 ˚C.

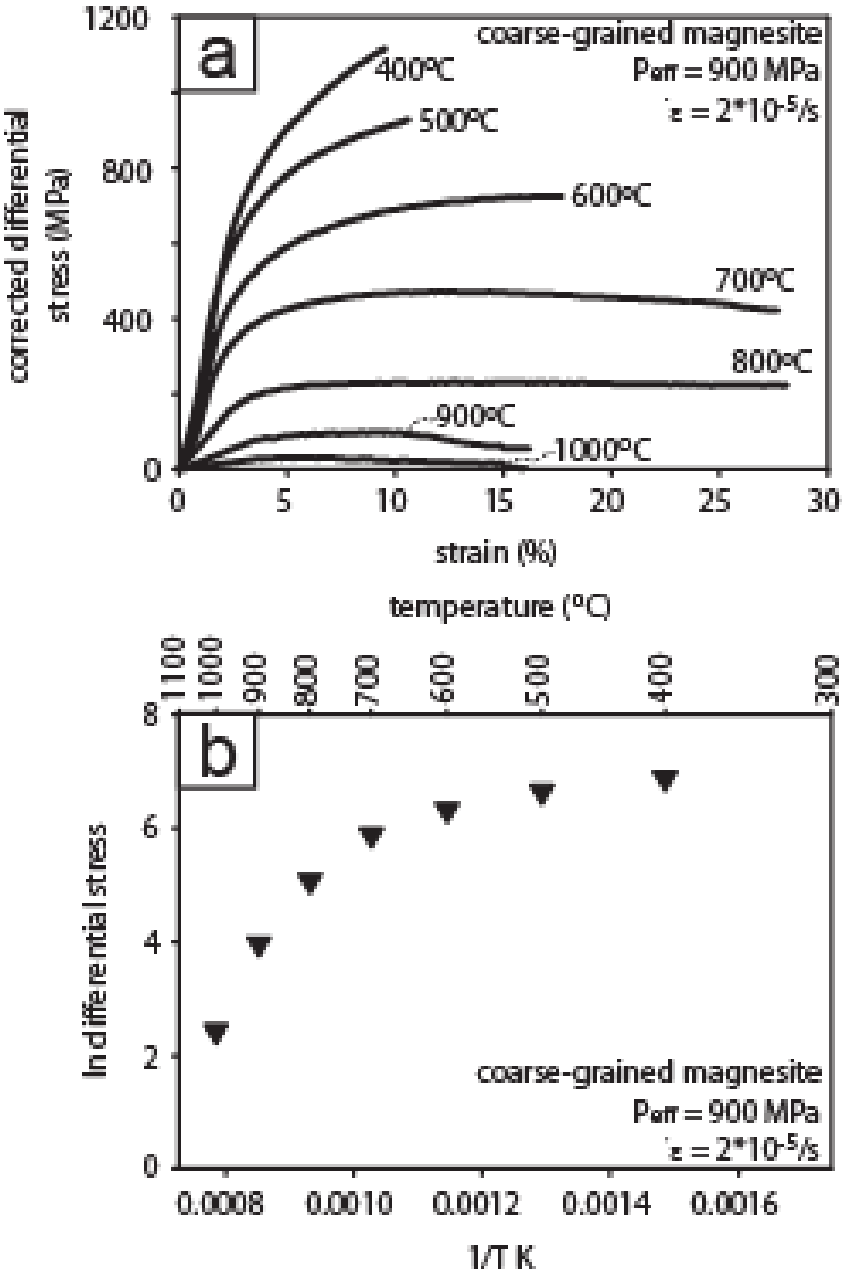

Figure 3: (a) Differential stresses decrease as a function of increasing temperature. Samples deformed at 400 and 500 ˚C strain-harden throughout deformation. Samples deformed at temperatures from 600-1000 ˚C strain-harden initially then deform at a constant differential stress. (b) Arrhenius relationship identifies two distinct linear trends. The slope of the line of samples deformed at temperatures from 400-600 ˚C is indicative of low-temperature crystal plasticity. The slope of the line of samples deformed at tepreatures from 700-1000˚C is indicative of dislocation creep.

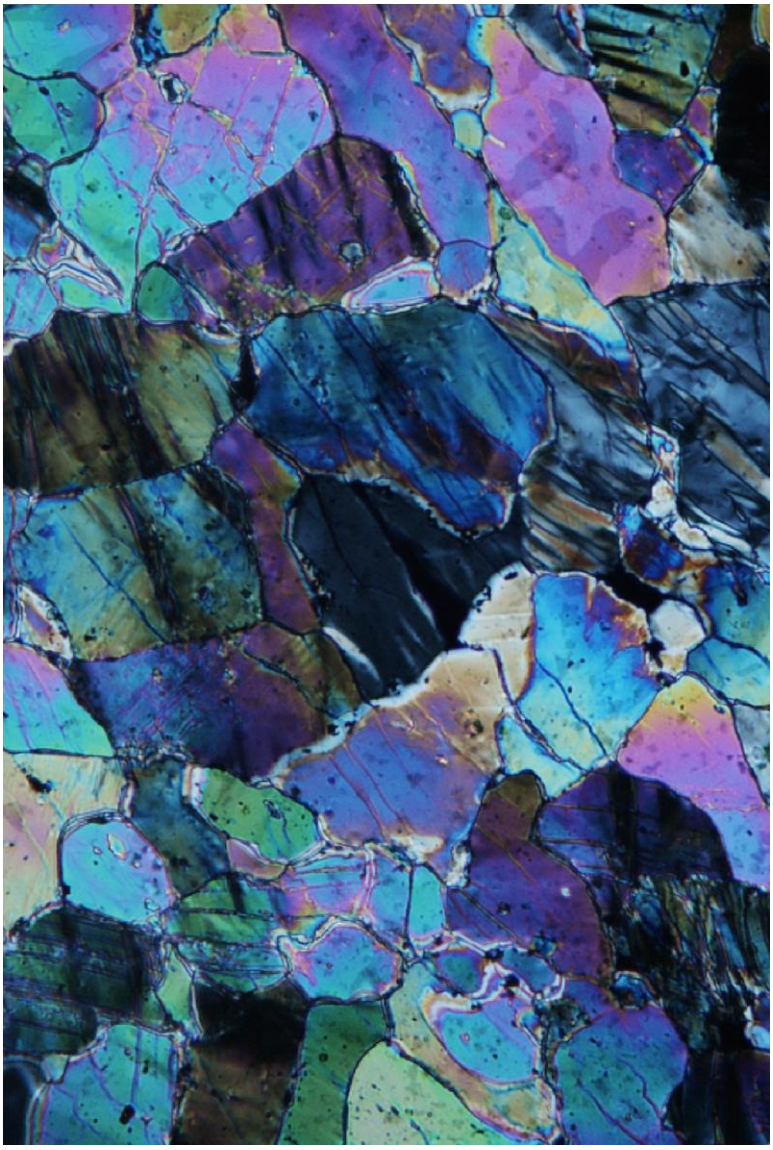

Figure 4: Photomicrograph of the sample deformed at 400 ˚C. σ_1 oriented in the vertical direction. Grains exhibit twinning, kink bands, and undulatory extinction.

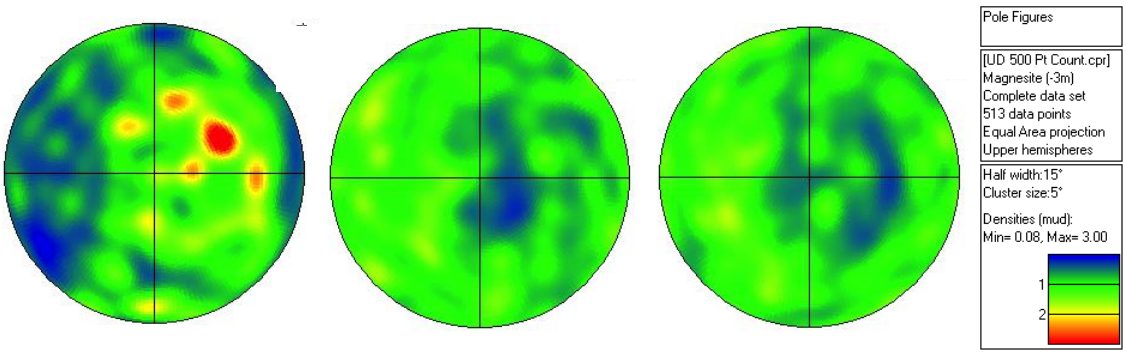

Figure 5: Crystallographic preferred orientation of the undeformed sample.

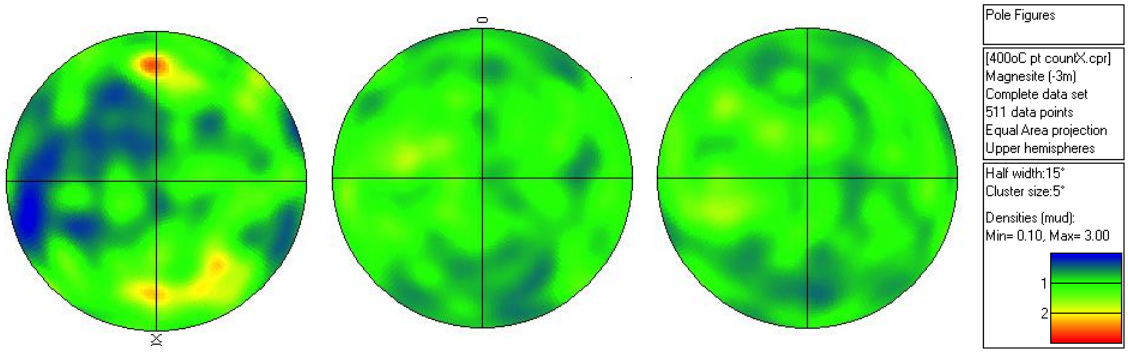

Figure 6: Crystallographic preferred orientation of the sample deformed at 400 ˚C. σ1 oriented in the vertical driection. Maxima allign obliquely with σ1.

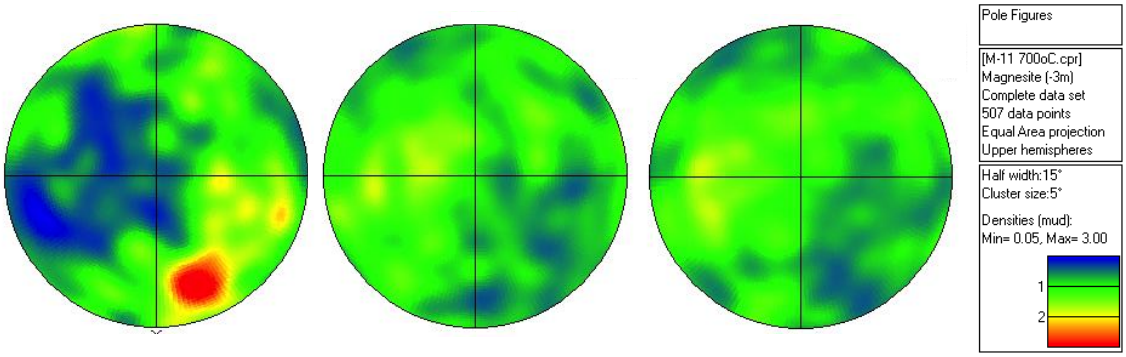

Figure 7: Crystallographic preferred orientation of the sample deformed at 600 ˚C. σ1 oriented in the vertical driection. Maxima allign obliquely with σ1 and are stronger than in the 400 ˚C sample.

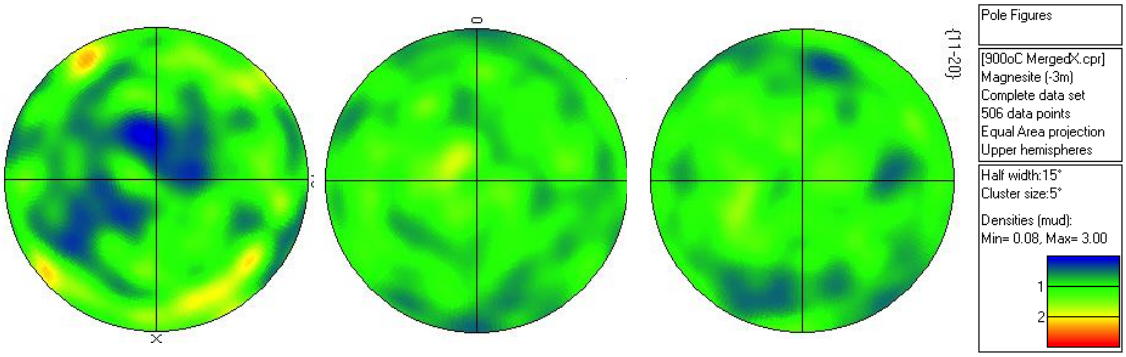

Figure 8: Crystallographic preferred orientation of the sample deformed at 700 ˚C. σ1 oriented in the vertical driection. Points form a girdle, as opposed to the maxima seen in the samples deformed at 400 and 600 ˚C.

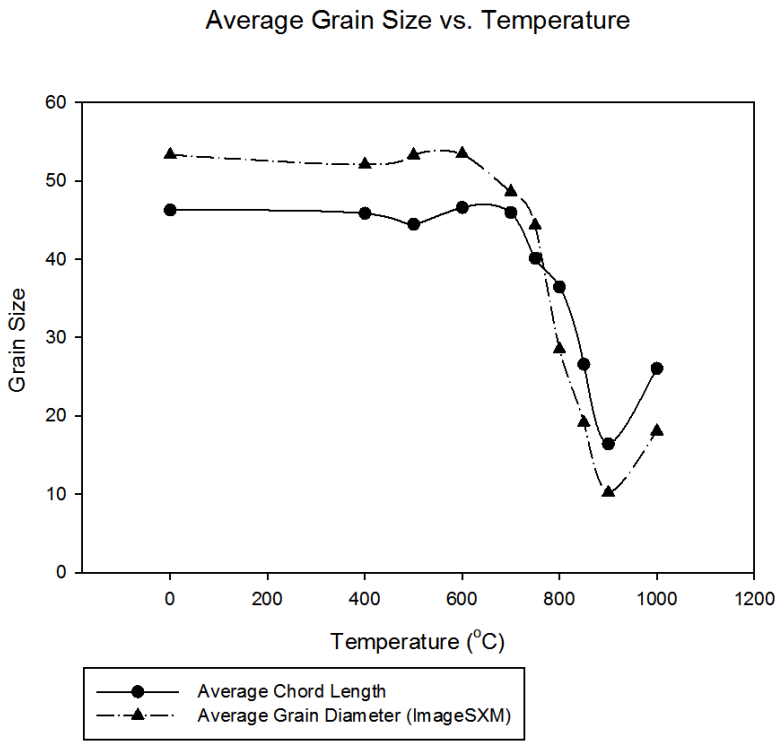

Figure 9: Host grain size stays relatively constant at temperatures < 750 ˚C. At temperatures > 700 ˚C grain size decreases as a function of both increasing temperature and strain.

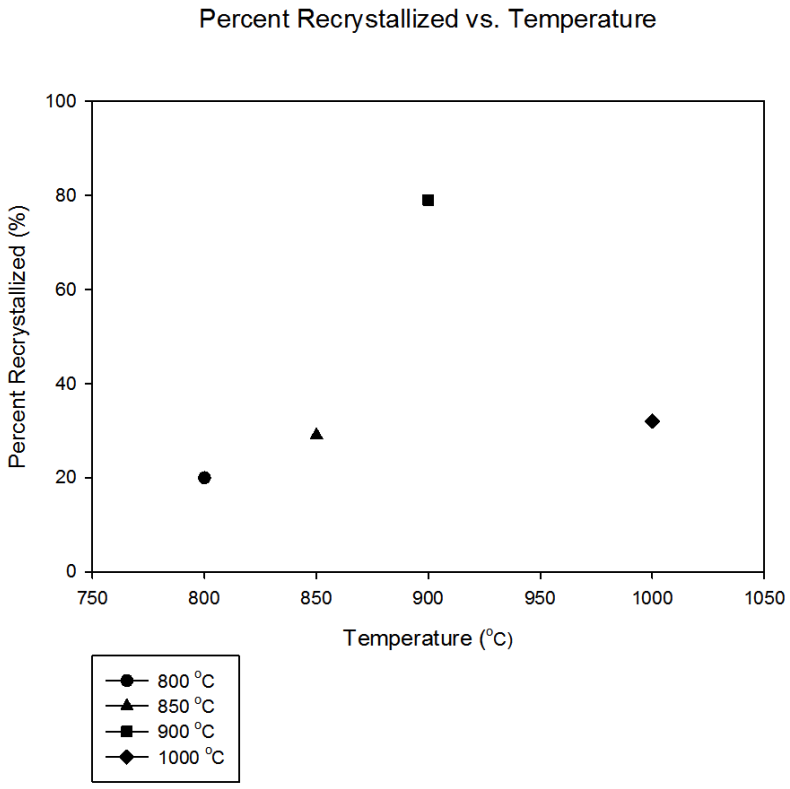

Figure 10: The percentage of the sample composed of recrystallized grains increases as a function of increasing temperature and strain.

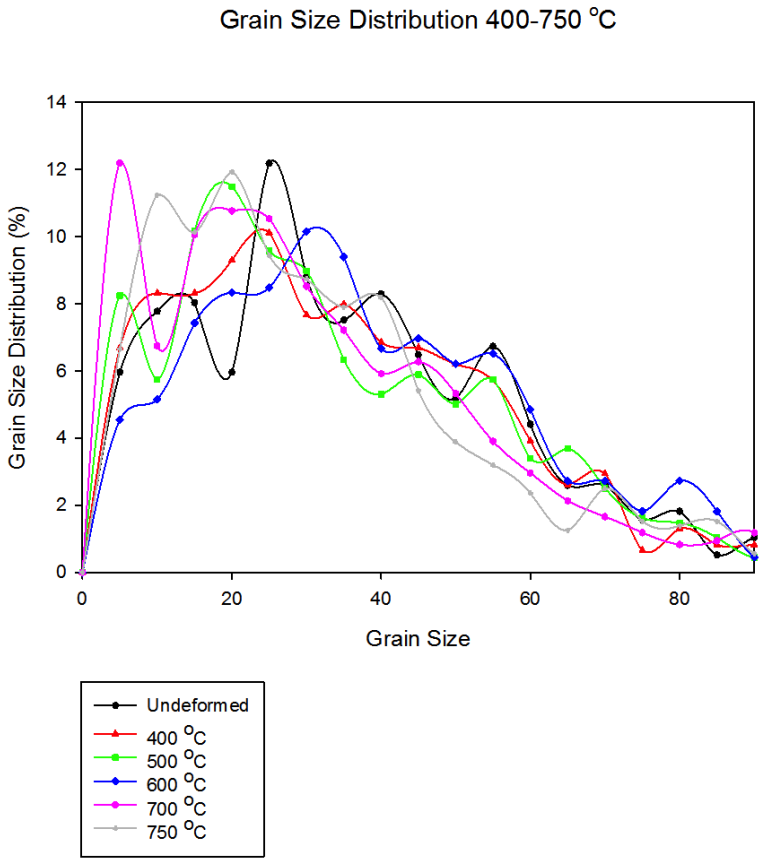

Figure 11: Spektor's chord analysis of samples deformed at temperatures from 400-750 ˚C. The majority of grains have an average chord length of ~50 µm.

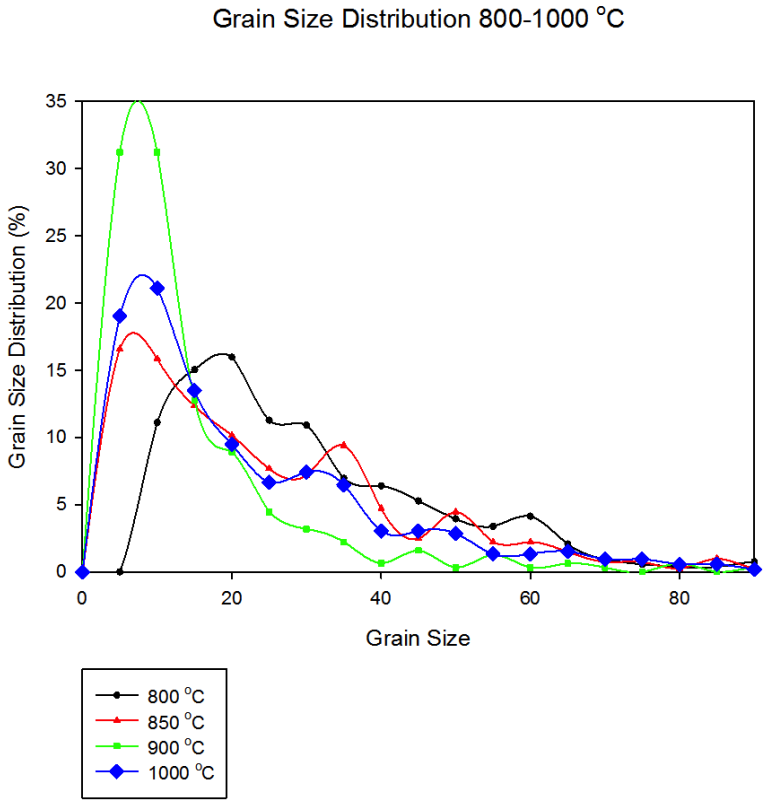

Figure 12: Spektor's chord analysis of samples deformed at temperatures from 800-1000 ˚C. The majority of host grains have an average chord length of ~15 µm.

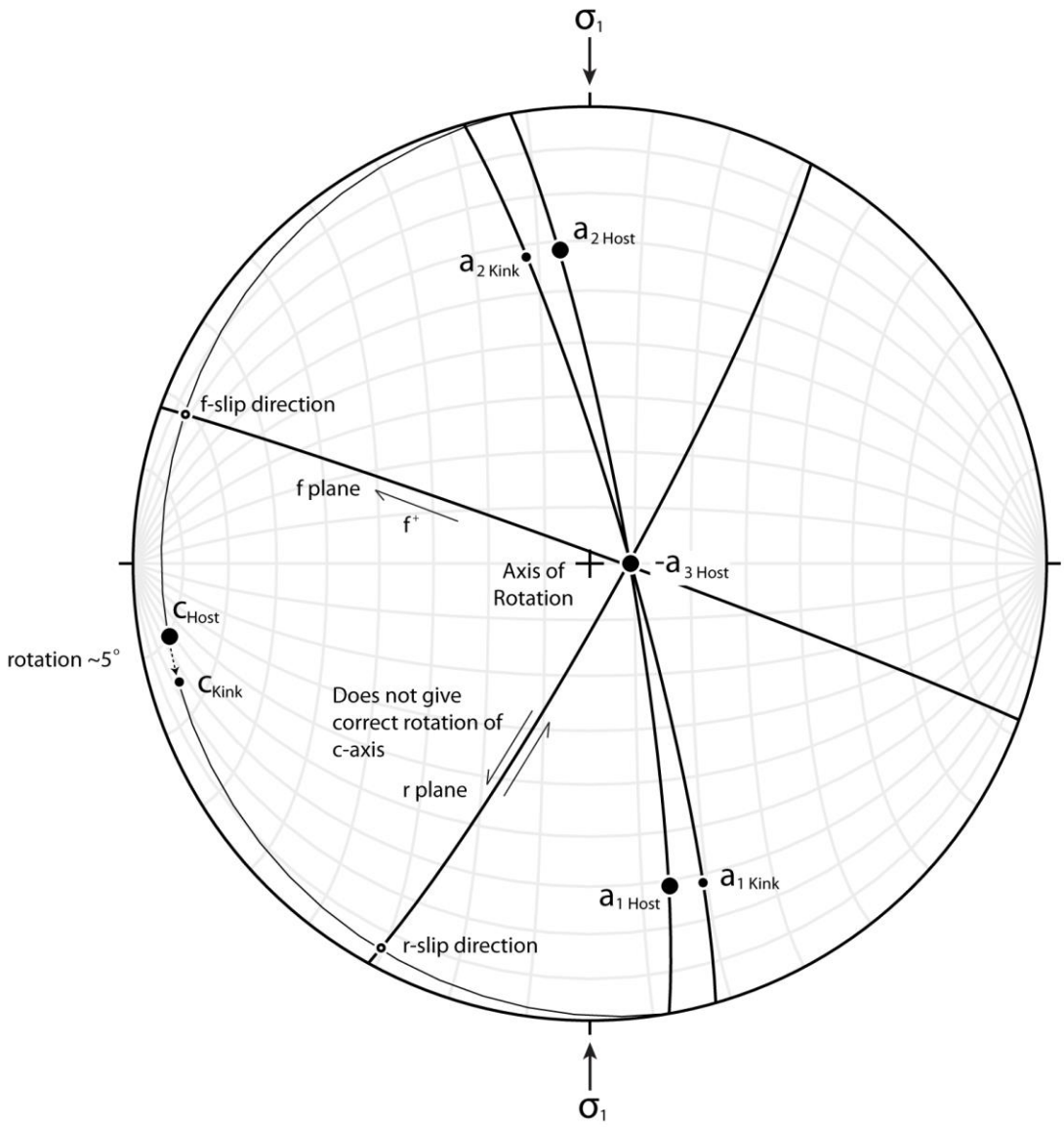

Figure 13: Slip systems were identified based on their axis of rotation. Slip on the r- and f- planes rotate about one of the a-axes. In this example, the kinked portion of the grain is rotated 24˚ from the host about the a-axis.

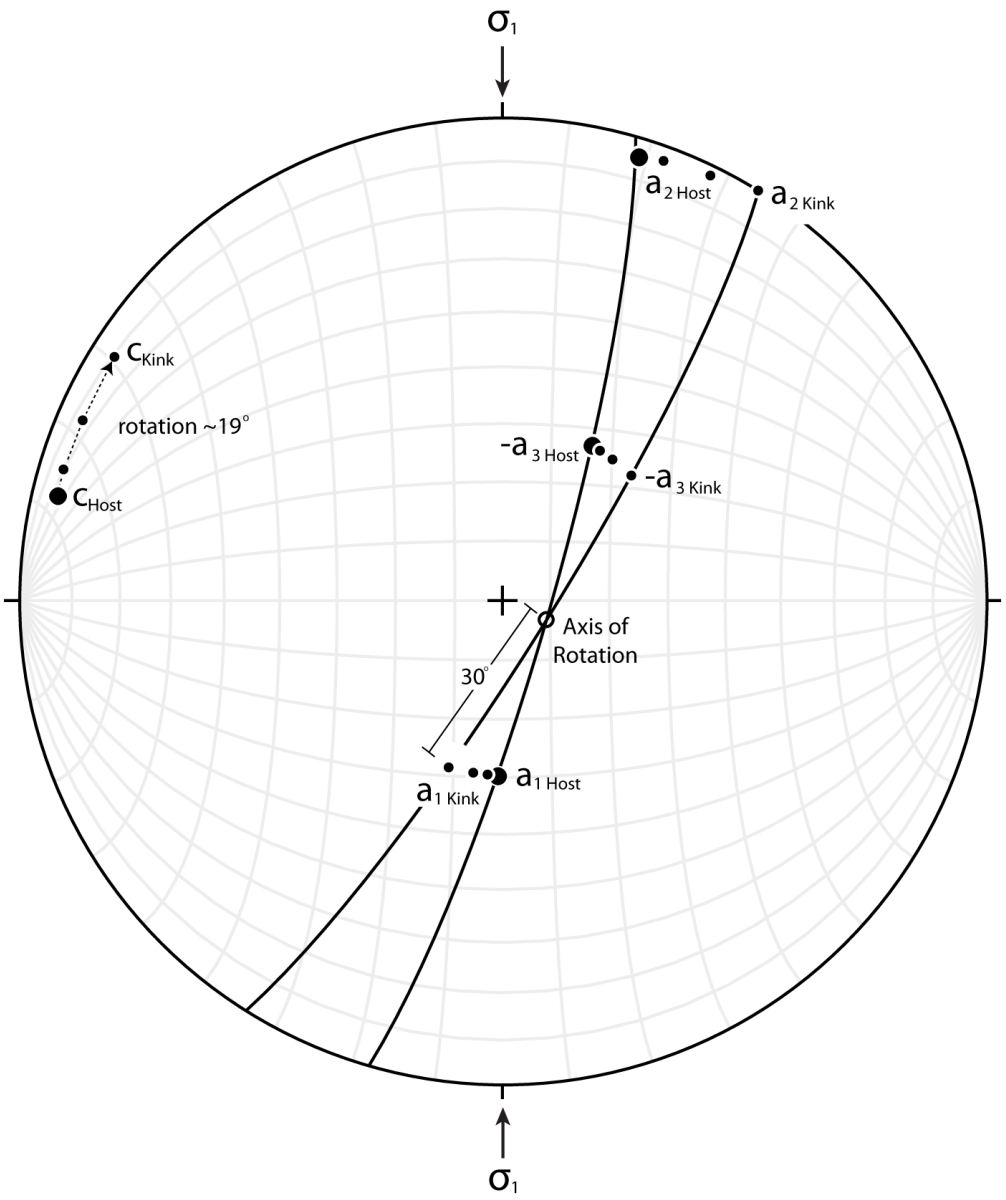

Figure 14: Slip systems were identified based on their axis of rotation. Slip on the c-axis rotates 30˚ from one of the a-axes. In this example, the kinked portion of the grain is rotated 19˚ from the host about the a-axis.

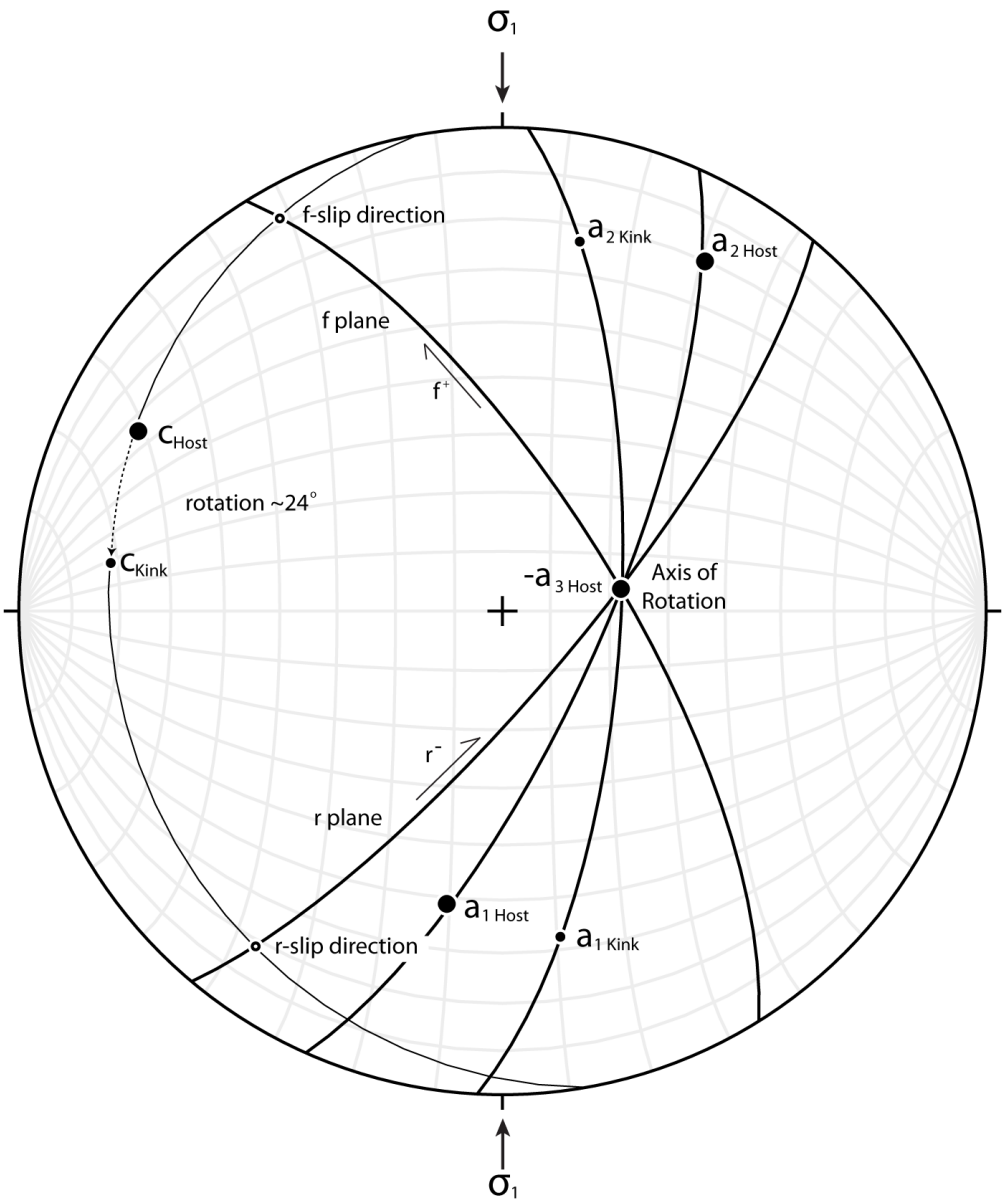

Figure 15: Slip systems were identified based on their axis of rotation. Slip on the r- and f- planes rotate about one of the a-axes. In this example, the kinked portion of the grain is rotated 5˚ from the host about the a-axis. Based on the orientation and rotation of the grain, r-slip was determined to be the only possible rotation.

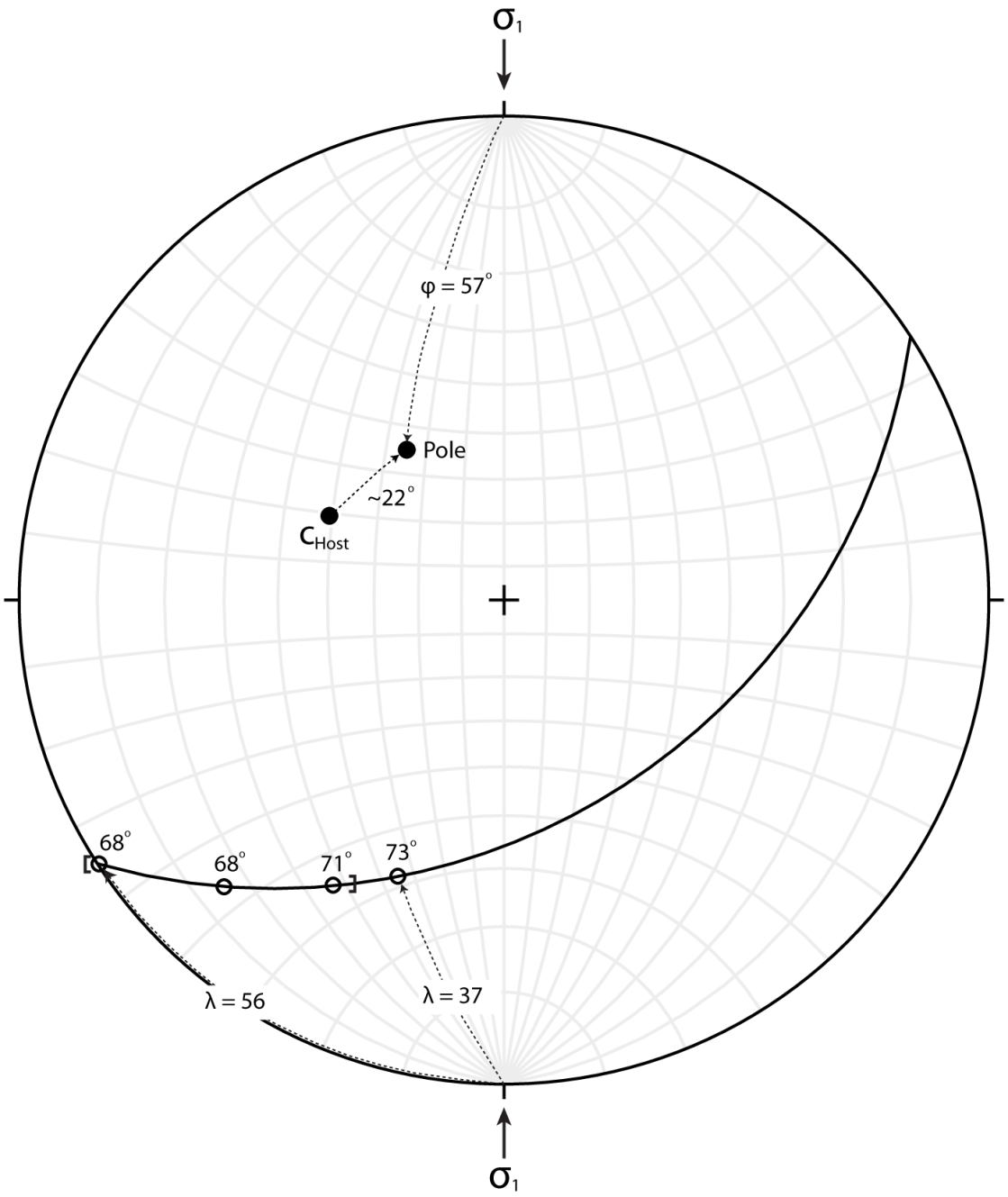

Figure 16: Twin from M-14, deformed at 400 °C. Schmid factors of twins were used to calculate the critical resolved shear stresses. These were identified by determining the angle (ψ) between σ_1 and the vector normal to the slip plane and, the angle (λ) between σ_1 and the slip direction.

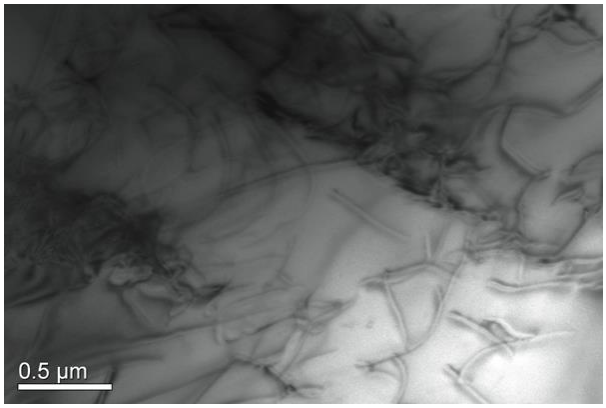

Figure 17: TEM image of a twin within a magnesite grain deformed at 400 ˚C. Twin boundaries are defined by the linear arrays of dislocations.

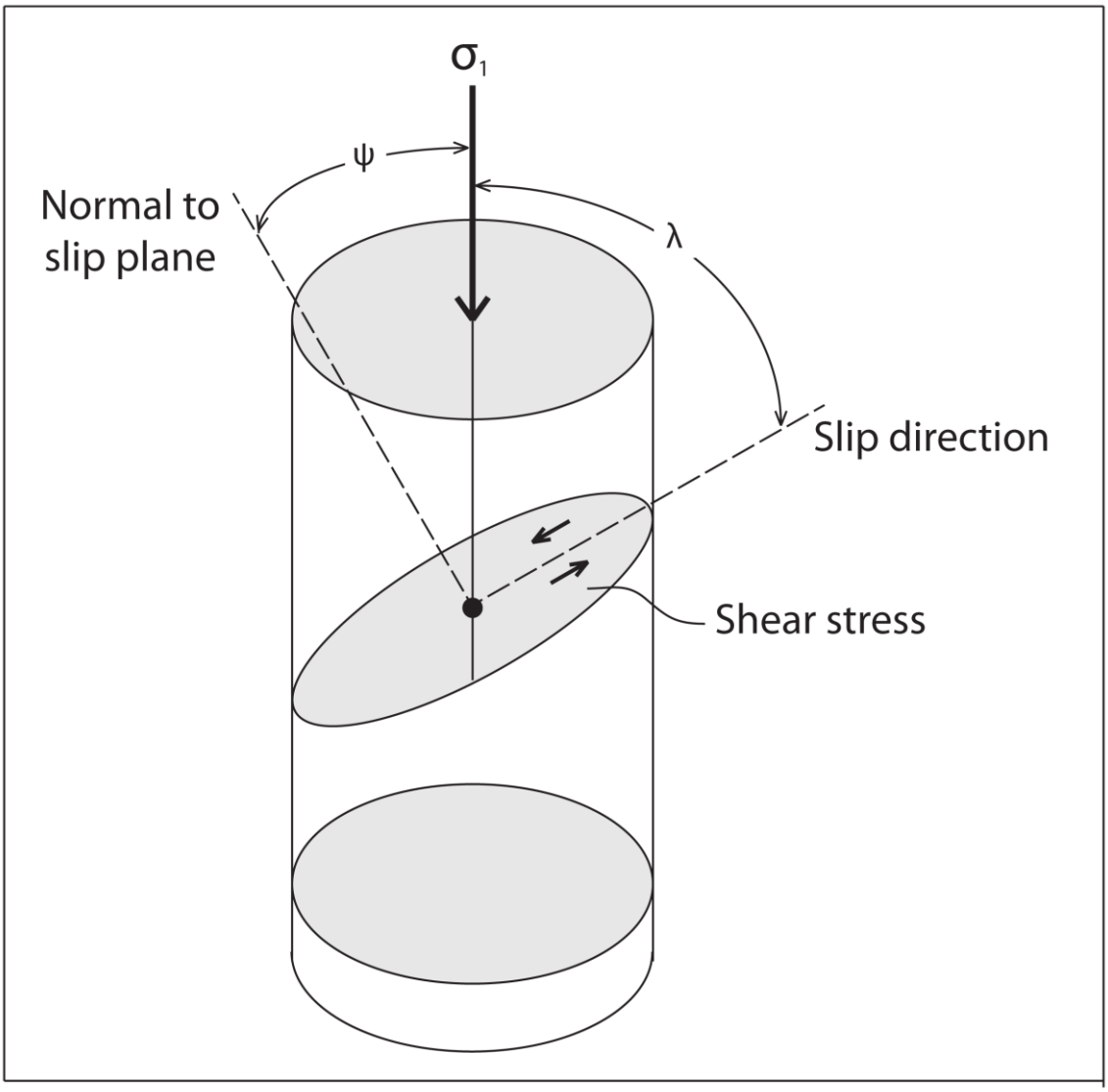

Figure 18: Schematic showing how Schmid factors are identified in twinned grains. Determining the angle (ψ) between σ_1 and the vector normal to the slip plane and, the angle (λ) between σ_1 and the slip direction are necessary.

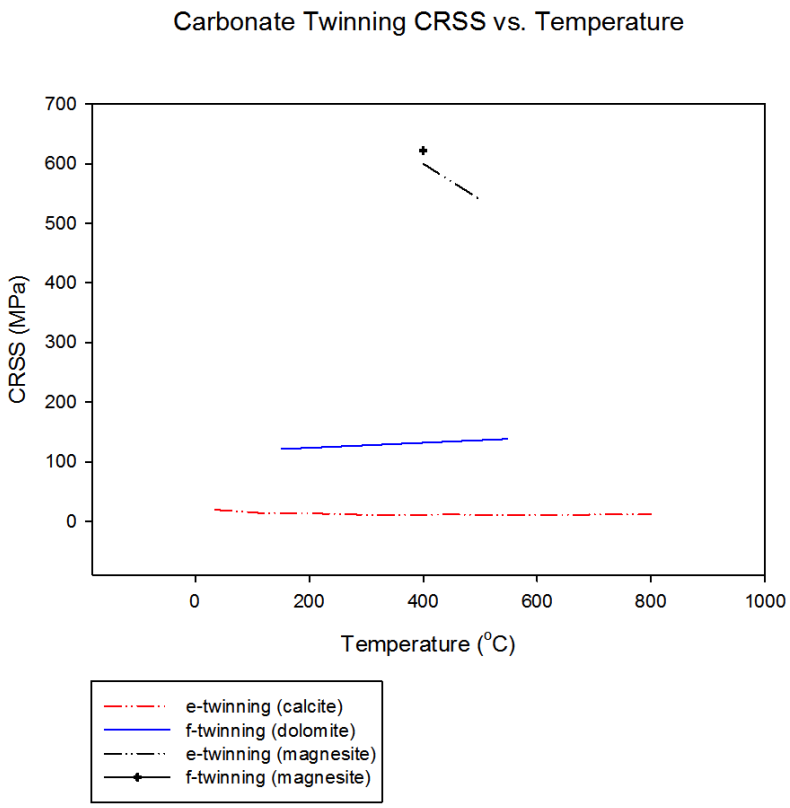

Figure 19: Critically resolved shear stresses of twins of calcite, dolomite, and magnesite. Magnesite twin critically resolved shear stresses are stignificantly greater than in calcite or dolomite twins.

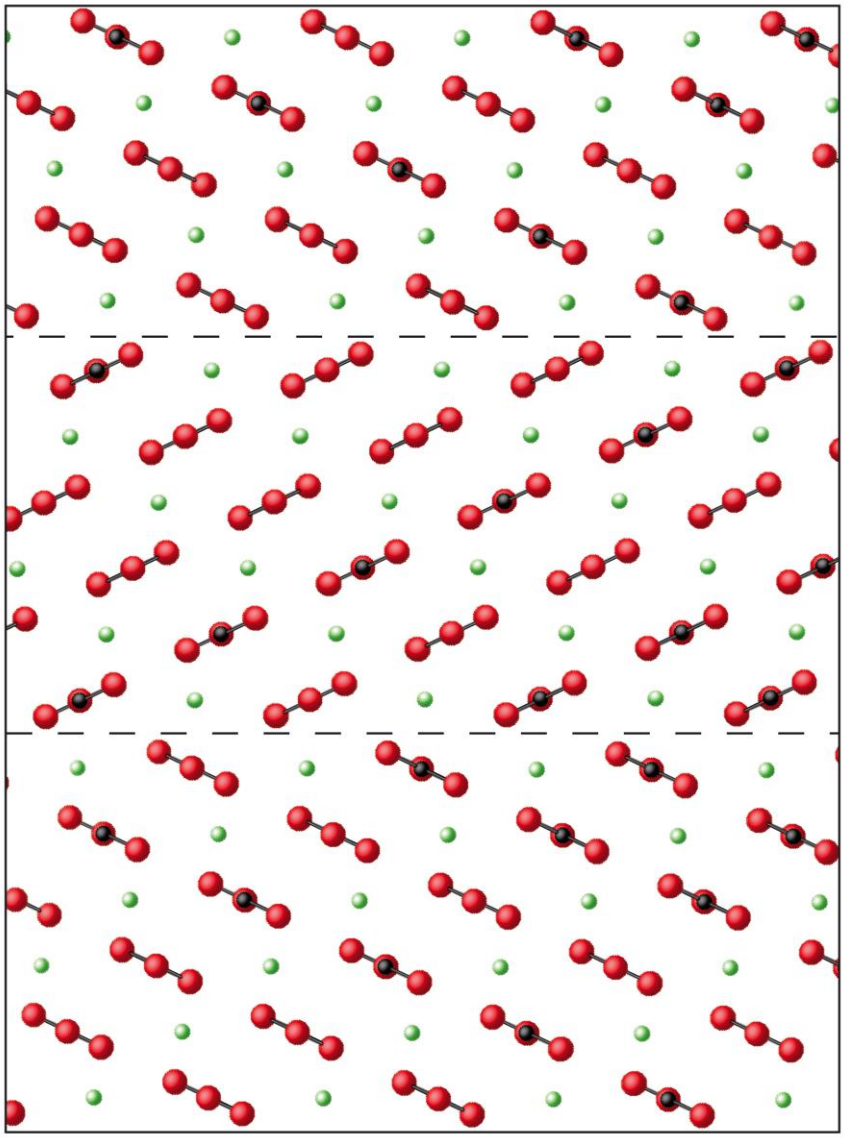

Figure 20: Model of an e-twin in magnesite based on *ab initio* models by Bruno et al. (2010).

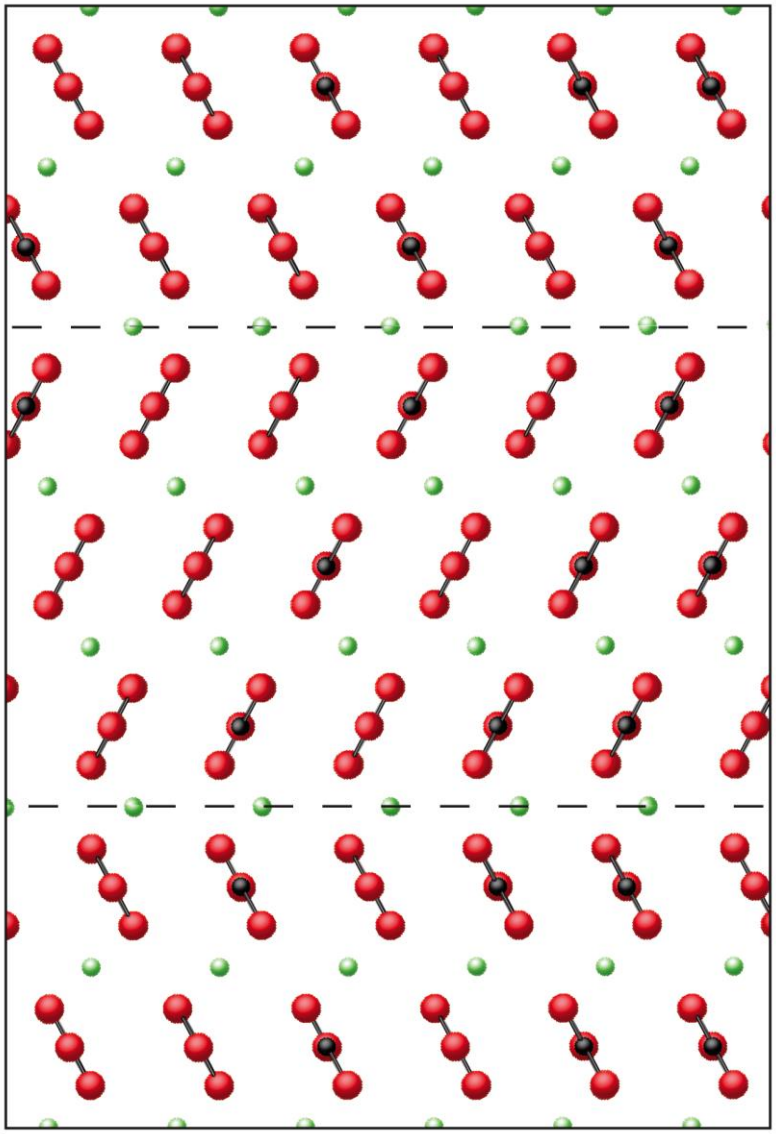

Figure 21: Model of an f-twin in magnesite based on *ab initio* models by Bruno et al. (2010).

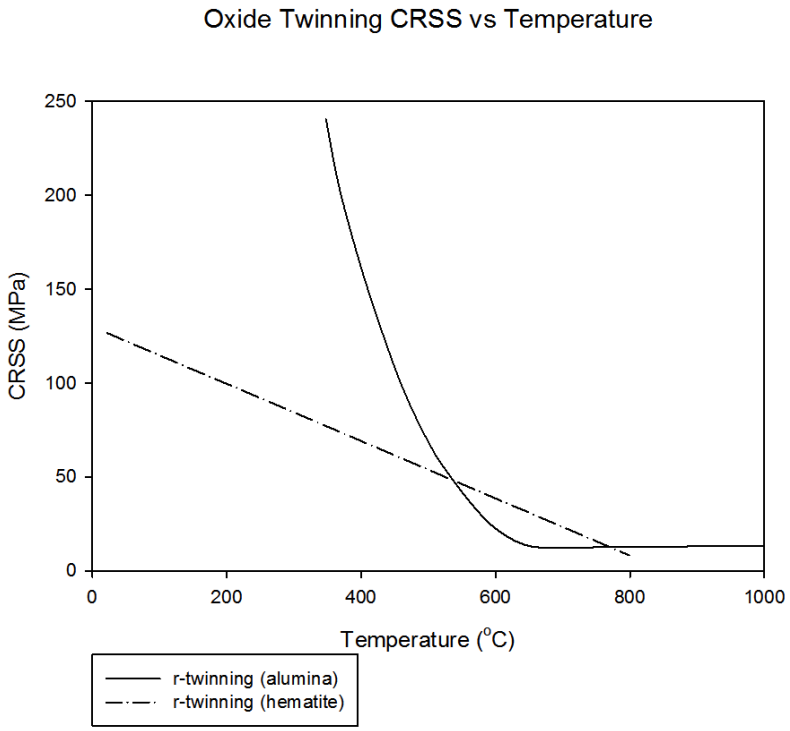

Figure 22: Critically resolved shear stresses of r-twins in alumina and hematite. Alumina strength is significantly greater than that of hematite.

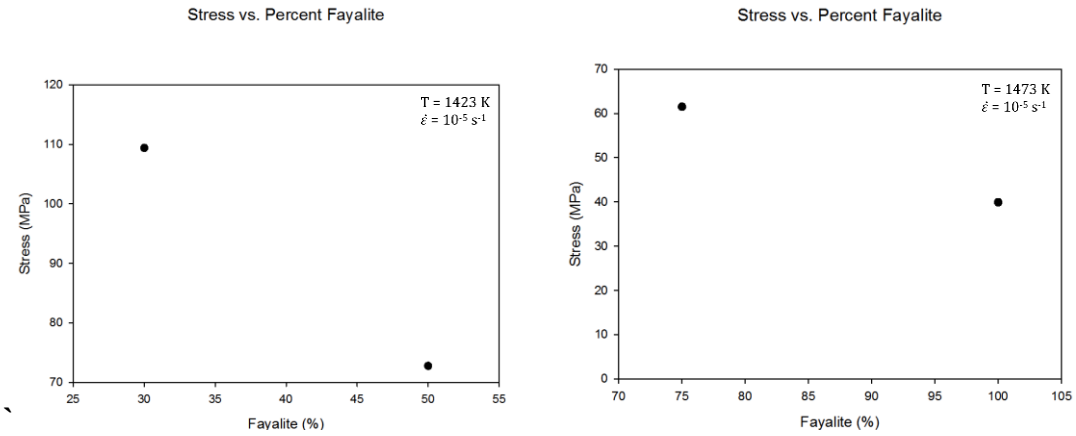

Figure 23: Stresses of dislocation glide in olivine grains of differing chemical compositions. Samples contatining higher percentages of forsterite have higher differential stresses required for slip.